



**HAL**  
open science

## Synthesis and properties of carbon microspheres based on tannin-sucrose mixtures treated in hydrothermal conditions

Angela Sanchez-Sanchez, Flavia L. Braghiroli, M.T. T Izquierdo, Julien Parmentier, Alain Celzard, V. Fierro

### ► To cite this version:

Angela Sanchez-Sanchez, Flavia L. Braghiroli, M.T. T Izquierdo, Julien Parmentier, Alain Celzard, et al.. Synthesis and properties of carbon microspheres based on tannin-sucrose mixtures treated in hydrothermal conditions. *Industrial Crops and Products*, 2020, 154, pp.112564. 10.1016/j.indcrop.2020.112564 . hal-03041960

**HAL Id: hal-03041960**

<https://hal.univ-lorraine.fr/hal-03041960v1>

Submitted on 5 Dec 2020

**HAL** is a multi-disciplinary open access archive for the deposit and dissemination of scientific research documents, whether they are published or not. The documents may come from teaching and research institutions in France or abroad, or from public or private research centers.

L'archive ouverte pluridisciplinaire **HAL**, est destinée au dépôt et à la diffusion de documents scientifiques de niveau recherche, publiés ou non, émanant des établissements d'enseignement et de recherche français ou étrangers, des laboratoires publics ou privés.



Distributed under a Creative Commons Attribution - NonCommercial - NoDerivatives 4.0 International License

1  
2  
3                   Synthesis and properties of carbon  
4                   microspheres based on tannin-sucrose  
5                   mixtures treated in hydrothermal conditions

6  
7  
8           A. Sanchez-Sanchez<sup>1</sup>, F.L. Braghiroli<sup>1,2</sup>, M.T. Izquierdo<sup>3</sup>, J.  
9                           Parmentier<sup>4</sup>, A. Celzard<sup>1</sup>, V. Fierro<sup>\*1</sup>

10  
11  
12           <sup>1</sup> Université de Lorraine, CNRS, IJL, F-88000 Epinal, France

13  
14           <sup>2</sup> Centre Technologique des Résidus Industriels (CTRI), Cégep de l'Abitibi-Témiscamingue,  
15           425 Boul. du Collège, Rouyn-Noranda, QC J9X 5E5, Canada

16  
17           <sup>3</sup> Instituto de Carboquímica, ICB-CSIC, Miguel Luesma Castán, 4. 50018 Zaragoza, Spain

18  
19           <sup>4</sup> Université de Haute Alsace, Institut de Science des Matériaux de Mulhouse, LRC CNRS  
20           7228, 15 rue Jean Starcky, BP 2488, 68057 Mulhouse Cedex, France

21  
22  

---

\* Corresponding author. Tel: + 33 329 29 61 77. Fax: + 33 329 29 61 38. E-mail address :  
[Vanessa.Fierro@univ-lorraine.fr](mailto:Vanessa.Fierro@univ-lorraine.fr) (V. Fierro)

## 23 Abstract

24 Sustainable carbon materials have been synthesised by use of inexpensive natural  
25 precursors, tannin and sucrose, mixed in aqueous solution in various proportions (from 0:1 to  
26 1:0), and then submitted to hydrothermal carbonisation (HTC) at various pH (from 2 to 8) and  
27 temperatures (160, 180 or 200°C). The resultant hydrochars were finally pyrolysed at 900°C  
28 under nitrogen flow to produce highly porous carbon materials with BET areas as high as 810  
29 m<sup>2</sup>/g without activation. The effects of the initial tannin/sucrose weight ratios and of the HTC  
30 conditions were investigated in terms of final particle size (from 1 to 10 µm), carbon yield  
31 (from 30 to 45%), composition (C from 88 to 93 wt. %; O from 6 to 10 wt. %), surface  
32 chemistry (C from 88 to 98 at. %; O from 2 to 12 at. %) and porous texture (NLDFT surface  
33 areas and micropore volumes from 840 to 1420 m<sup>2</sup>/g and from 0.23 to 032 cm<sup>3</sup>/g,  
34 respectively). All these parameters were discussed and correlated with the electrochemical  
35 properties of the same materials. Special attention was paid to the separate roles of porosity  
36 and surface chemistry, and on the reversibility of the electrochemical reactions.

37

38

39

40

41

42

43 **Keywords:** Tannin; Sucrose; Hydrothermal Carbonisation; Sustainable Carbons;  
44 Supercapacitor electrodes.

45

## 46 **1. Introduction**

47 Carbon materials are applied to several fields of paramount importance such as catalysis,  
48 water and air depollution, and energy storage and conversion such as secondary batteries or  
49 supercapacitors. The production of “sustainable carbon materials” from inexpensive carbon  
50 sources including lignocellulosic biomass or other by-products contained in food/agricultural  
51 waste, is of major importance nowadays. One way of achieving this target and producing  
52 functionalised carbon materials is applying hydrothermal carbonisation (HTC) as a low-cost,  
53 scalable, and industrially attractive first step of carbonisation prior to pyrolysis (Antonietti  
54 and Titirici, 2010; Celzard et al., 2012; Hu et al., 2010). HTC maintains high oxygen content  
55 and allows the functionalisation of the resultant materials without the need of additional  
56 chemical reagents (Unur, 2013). The use of moderate temperature and pressure conditions are  
57 fundamental for the onset of several reactions to which carbohydrates are submitted such as  
58 hydrolysis, dehydration, condensation, aromatisation and polymerisation (Sevilla and Fuertes,  
59 2009). An insoluble black solid that contains higher carbon content than in the original  
60 material is obtained, and then a second-step of pyrolysis at 900°C can be applied for  
61 increasing the electrical conductivity and improving the textural properties of the final  
62 materials.

63 HTC has been applied to a broad range of carbohydrates and biomass: rice grains, oak  
64 leaves, pine needles (Titirici et al., 2007), microalgae (Falco et al., 2012) and prawn shells  
65 (White et al., 2009). Mimoso tannin has also been submitted to HTC. Mimoso tannin is a  
66 phenolic material that has been used for the production of several materials such as  
67 resins/adhesives (Pizzi, 1994), foams (Tondi et al., 2009; Letellier et al., 2017), gels  
68 (Szcurek et al., 2011a, 2011b) and recently N-doped carbon materials (Braghiroli et al.,  
69 2012, 2015a). This is explained by the fact that such condensed (flavonoid) tannins are quite  
70 reactive in the presence of aldehydes (e.g. formaldehyde), and another advantage is that they

71 can auto-condensate, especially when heated or in presence of strong mineral acids (Pizzi,  
72 1983). Fig. 1 shows the main flavonoid structure of the robinetinidol unit (resorcinol A-ring  
73 and pyrogallol B-ring) which constitutes approximately 70% of Mimosa tannin extract (Bate-  
74 Smith, 1962; Pizzi, 1983; Hemingway et al., 1989; Pizzi, 1994).

#### 75 Figure 1

76 Various carbonaceous microspheres were obtained after tannin HTC, depending on  
77 temperature, reaction time and tannin concentration, and their production was found to obey a  
78 first-order kinetics with an activation energy of  $91 \text{ kJ mol}^{-1}$  (Braghiroli et al., 2014). The  
79 mechanism of microspheres formation proceeds by nucleation, leading to a high number of  
80 small particles, followed by growth and coalescence, leading to bigger particles of lower  
81 surface area. The hydrochar yield investigated as a function of pH was found to increase from  
82 64.4 % at unmodified pH (around 4.2 for the aqueous tannin solution) to 86.7 % when the pH  
83 was decreased to 1. The pH also influenced the morphology and the texture of the hydrochars,  
84 those prepared at non-modified pH being powders, whereas those obtained at low pH being  
85 stiff monoliths presenting a higher surface area, up to  $800 \text{ m}^2 \text{ g}^{-1}$  after pyrolysis at  $900^\circ\text{C}$ . But  
86 in all cases, the micropore size distributions were the same (Braghiroli et al., 2015b).

87 Concerning sugars, Wang et al. (2001) submitted a sucrose solution ( $1.5 \text{ mol L}^{-1}$ ) to HTC  
88 at  $190^\circ\text{C}$  during 5h to produce carbonaceous microspheres with an average diameter of  $5 \mu\text{m}$   
89 and a BET area as high as  $400 \text{ m}^2 \text{ g}^{-1}$  after subsequent pyrolysis at  $1000^\circ\text{C}$ . Then, Sevilla and  
90 Fuertes (2009) studied the hydrochars obtained after HTC of several saccharides in different  
91 conditions of temperature ( $170\text{-}240^\circ\text{C}$ ) and reaction time (0.5-15h) concluding that they  
92 presented a core-shell structure consisting of a hydrophobic core and a hydrophilic shell  
93 containing reactive oxygenated functional groups. Next, Falco et al. (2012) observed the  
94 effect of adding glucose to microalgae organisms submitted to HTC, and found that such

95 strategy allowed incorporating nitrogen in the final carbon matrix and also increasing the  
96 carbon yield from 18 to 47.5%.

97 In the present study, we used condensed tannin combined with commercial sugar (sucrose)  
98 to see the effects of such mixture on the preparation of carbon materials. Sucrose was selected  
99 because it is a commercial product, readily available and not expensive but also for  
100 comparison purposes with previous studies (Wang et al., 2001; Sevilla and Fuertes, 2009).  
101 Various kinds of microspheres were seen by electron microscopy, depending on temperature,  
102 pH, and sucrose / tannin ratio. After a subsequent thermal treatment at 900°C, the final carbon  
103 materials presented developed textural properties especially at low pH. To understand better  
104 the influence of the various chemical and structural characteristics of the present carbons,  
105 some of them were tested as electrode materials and the reversibility of the oxygen groups'  
106 reactions in acidic electrolyte was studied. Such electrochemical studies allowed separating  
107 the roles of the materials' features, and suggesting how to improve further their capacitance if  
108 we were to start developing supercapacitor electrodes.

109

## 110 **2. Materials and methods**

### 111 2.1 Raw materials

112 Mimosa tannin, kindly supplied by SilvaChimica, was used in this study. The extraction  
113 process and the composition of the tannin extract was described elsewhere (Braghiroli et al., 2014).

### 114 2.2 Hydrothermal treatment

115 In a typical synthesis, 2.0 g of either tannin (T) alone, sucrose (S) alone, or tannin-sucrose  
116 mixture, were dissolved in 16.0 g of water, put inside a glass vial and then into a Teflon-lined  
117 autoclave for 24h installed in an oven preheated at 180°C. Different conditions of  
118 hydrothermal carbonisation (HTC) were studied, using various fractions of sucrose: 0, 25, 50,

119 75 and 100 wt. %. The addition of sucrose changed the pH from 4.2 (100% T) to 8 (100% S).  
120 The resultant materials were called HsStT180\_u, s and t being the percentages of sucrose and  
121 tannin, respectively, and u meaning unmodified pH. A second series of samples was prepared  
122 by fixing the pH at 2 by use of pTSA. Those materials were labelled HsStT180\_2. The HTC  
123 temperatures were also varied, 160 or 200°C, and the corresponding samples were labelled  
124 HsStT160\_u or HsStT200\_u for unmodified pH experiments.

125 In all cases, the filtrates were recovered, washed with water, and then dried in a vacuum  
126 oven at 80°C. Pyrolysis was carried out under nitrogen flow in a tubular furnace heated at 1°C  
127 min<sup>-1</sup> up to 900°C, and this temperature was hold for 3h. Pristine tannin (OS100T) was also  
128 carbonised in the same conditions and labelled C0S100T. In order to distinguish carbon  
129 materials from hydrochars, we added a 'C' at the beginning of the label; for instance, the  
130 sample H100T180\_2 became CH100T180\_2 after pyrolysis at 900°C.

### 131 2.3 Materials characterisation

132 Scanning electron microscopy (SEM) observations were carried out with a FEI-Quanta 400  
133 apparatus for investigating the morphology of the samples, which were metallised beforehand.  
134 A series of images was taken for each sample, and only one was provided here as an example.  
135 The purpose was to evaluate the morphology of the samples and to observe general trends in  
136 the particle size, depending on the preparation conditions.

137 Pore texture parameters were obtained by krypton adsorption at -196°C for organic, or  
138 non-porous samples obtained after HTC, and by nitrogen adsorption at -196°C for pyrolysed  
139 materials, using a ASAP 2020 automatic apparatus (Micromeritics) in both cases. CO<sub>2</sub>  
140 adsorption at 0°C was also carried out on pyrolysed samples using a Micromeritics ASAP  
141 2420 apparatus. The following parameters were determined: NLDFT surface area,  $S_{NLDFT}$  (m<sup>2</sup>  
142 g<sup>-1</sup>); BET area,  $A_{BET}$  (m<sup>2</sup> g<sup>-1</sup>); total pore volume,  $V_{0.97}$  (cm<sup>3</sup> g<sup>-1</sup>); micropore volumes,  $V_{DR,N2}$

143 and  $V_{DR,CO_2}$  ( $\text{cm}^3 \text{g}^{-1}$ ), from the  $\text{N}_2$  or  $\text{CO}_2$  adsorption isotherms; micropore volume,  $V_{\mu,NLDFT}$   
144 ( $\text{cm}^3 \text{g}^{-1}$ ), by applying the 2D- NLDFT-HS to both  $\text{CO}_2$  and  $\text{N}_2$  adsorption isotherms; and  
145 mesopore volume,  $V_{mes}$  ( $\text{cm}^3 \text{g}^{-1}$ ), calculated as the difference  $V_{0.97} - V_{DR,N_2}$ . The pore size  
146 distributions (PSDs) were calculated by applying the 2D-NLDFT-HS method to both  $\text{CO}_2$  and  
147  $\text{N}_2$  adsorption isotherms. More details are given elsewhere (Schaefer et al., 2016).

148 Ultimate analyses of samples were carried out in a CHONS elemental analyser (Vario El  
149 cube, Elementar) as reported elsewhere (Celzard et al., 2019). Temperature-Programmed  
150 Desorption (TPD) experiments were performed with a custom-built set-up, consisting of a  
151 tubular quartz reactor placed inside an electric furnace. In a typical experiment, the sample  
152 was heated up to  $1100^\circ\text{C}$  in Ar atmosphere at a heating rate of  $10^\circ\text{C min}^{-1}$ . The amounts of  
153 CO and  $\text{CO}_2$  were determined as reported elsewhere (Tellez-Juárez et al., 2014).

154 X-ray photoelectron spectroscopy (XPS) results were recorded with an ESCAPlus  
155 OMICROM system equipped with a hemispherical electron energy analyser. Measurements  
156 were carried out as reported elsewhere (Sanchez-Sanchez et al., 2018).

157 Electrochemical characterisation was performed with a Biologic VMP3 multi-potentiostat.  
158 The carbon electrodes were prepared by spreading onto a graphite foil a paste ( $\sim 15 \text{ mg cm}^{-2}$ )  
159 made of the carbon material mixed with polytetrafluoroethylene (PTFE) binder and carbon  
160 black in the weight percent ratio of 85:10:5. The resulting electrodes were then pressed at 5  
161 MPa and impregnated by  $1 \text{ mol L}^{-1} \text{H}_2\text{SO}_4$  electrolyte during 48 hours. Cyclic voltammetry  
162 (CV) tests were carried out at different scan rates between 0.5 and  $100 \text{ mV s}^{-1}$  and within the  
163 potential window of 0 – 0.8 V in a three-electrode cell, using a platinum gauze as the counter  
164 electrode and a saturated calomel electrode (SCE) as the reference one. The specific  
165 capacitance ( $C$ ,  $\text{F g}^{-1}$ ) was calculated from the CV curves according to Eq. (1):

$$166 \quad C = (\int I dV) / (s \Delta V m) \quad (1)$$



167 where  $I$  (A) is the current,  $s$  ( $\text{V s}^{-1}$ ) is the scan rate,  $\Delta V$  (V) is the potential window and  $m$  (g)  
168 is the mass of carbon in the electrode.

### 169 3. Results and discussion

#### 170 3.1 Carbon yields and morphologies

171 To study the effects of the pH on the tannin / sucrose solution submitted to HTC, the same  
172 weight (1 g) of sucrose and tannin was used. Table 1 shows the main characteristics of these  
173 hydrochars (H50S50T) at different pH ranging from 1 to unmodified (4.2). Unlike H0S100T  
174 (100% tannin submitted to HTC - see Fig. 2), submitting 50S50T to HTC at different pH did  
175 not produce any change in the HTC yield. Being at the level of  $61.5 \pm 1.5$  wt. %, the HTC  
176 yield of 50S50T was also always much lower than that of H0S100T. The  $A_{BET}$  values (around  
177  $1 \text{ m}^2 \text{ g}^{-1}$ ) were almost the same for 0S100T, H0S100T and H50S50T, considering the intrinsic  
178 uncertainties of adsorption techniques as soon as very low surface areas are concerned.  
179 Therefore, it can be concluded that, after HTC, the materials were not porous.

180 After a second thermal treatment at  $900^\circ\text{C}$ ,  $A_{BET}$  increased from  $471 \text{ m}^2 \text{ g}^{-1}$  for tannin  
181 directly pyrolysed (C0S100T) to  $639 \text{ m}^2 \text{ g}^{-1}$  for CH50S50T 180\_u (i.e., at unmodified pH),  
182 and even up to  $809 \text{ m}^2 \text{ g}^{-1}$  for CH50S50T 180\_1 (i.e., at pH 1). The increase of  $A_{BET}$  was also  
183 observed for the 100% tannin material (CH0S100T) having been submitted to HTC at low  
184 pH. Fig. 2 summarises the results of HTC yield and  $A_{BET}$  of all these hydrochars H0S100T  
185 and CH0S100T (already demonstrated in (Braghiroli et al., 2015b)) and H50S50T and  
186 CH50S50T at pH values ranging from 4 to 1. The results on pure tannin are presented here for  
187 the sake of comparison to study the effect of sucrose addition.

188 

189 It has already been mentioned that heating tannin in the presence of strong mineral acids  
190 favours its condensation/polymerisation reactions by different possible ways to form  
191 “phlobaphenes” or “tanner’s reds”, which are high-molecular weight, insoluble molecules  
192 (Pizzi, 1983; Braghiroli et al., 2015a). Tannin treated after HTC at  $180^\circ\text{C}$  was shown to have

193 a structure similar to that of flavonoid tannin (see [Fig. 1](#)), but presents a much higher level of  
194 polymerisation, mainly through the opening of the heterocyclic C2–ring and subsequent  
195 partial condensation between C2 (open) to C6 or C8, and partly through some auto-  
196 condensation C4 to C6 and C8 (Braghiroli et al., 2015a).

197 On the other hand, sucrose submitted to HTC undergoes hydrolysis that produces glucose  
198 and fructose, which decompose into hydroxymethylfurfural (HMF) as the main dehydration  
199 product, plus aldehydes (formaldehyde, pyruvaldehyde, etc.) and organic acids (acetic,  
200 formic, levulinic acids, etc.), hence producing a rapid pH change from 8 to 3 as shown in the  
201 literature (Antal et al., 1990; Ulbricht, 1984; Asghari and Yoshida, 2006). Glucose and  
202 fructose can also undergo polymerisation and condensation reactions as reported elsewhere  
203 (Antal et al., 1990; Kabyemela et al., 1997; Luijkx et al., 1995; Sevilla and Fuertes, 2009).  
204 Titirici et al. (2008) observed that the morphologies and chemical structures of carbons  
205 obtained from sucrose are directly related to those of carbons obtained from pure furan. It was  
206 also found that such intermediate molecules derived from saccharide dehydration as  
207 mentioned above coexist with furans and account for the observed changes of particle size,  
208 textural properties and particles aggregation.

209 When both materials (tannin and sucrose) coexist, we can assume that several reactive  
210 germs are obtained through hydrolysis of sucrose submitted to HTC. SEM photos show that  
211 the average microsphere diameter was reduced from 10  $\mu\text{m}$  for H0S100T (see [Fig. 3a](#)) to 2-5  
212  $\mu\text{m}$  by simple addition of sucrose (see [Fig. 3c](#)) for H50S50T, whereas 100% sucrose produced  
213 spheres of average size 1-2  $\mu\text{m}$  (see [Fig. 3b](#)). This finding suggests that sucrose reacts faster  
214 than tannin, producing more germs and, consequently, smaller spheres are obtained (see [Fig.](#)  
215 [3c](#)).

216

217 **Table 1:** Textural properties and elemental analysis obtained for materials 50S50T after HTC and subsequent pyrolysis made at different pH.

	Sample	Yield (wt. %)			Textural Properties						Elemental Analysis (wt. %)					
		HTC	Carbon	Total	$S_{NLDFT}$ ( $m^2 g^{-1}$ )	$A_{BET}$ ( $m^2 g^{-1}$ )	$V_{0.97}$ ( $cm^3 g^{-1}$ )	$V_{DR,N_2}$ ( $cm^3 g^{-1}$ )	$V_{DR,CO_2}$ ( $cm^3 g^{-1}$ )	$V_{\mu,NLDFT}$ ( $cm^3 g^{-1}$ )	C	H	N	S	O	C/O
No HTC	0S100T	-	-	-	-	0.27	-	-	-	-	53.8	5.4	0.6	0.1	40.1	1.3
After HTC	H0S100T180_u	64.6	-	-	-	0.78	-	-	-	-	60.9	4.4	0.8	0.0	33.8	1.8
	H50S50T180_1	63.0	-	-	-	1.22	-	-	-	-	62.6	5.0	0.6	0.2	31.6	2.0
	H50S50T180_2	60.0	-	-	-	1.05	-	-	-	-	62.6	4.3	0.2	0.2	32.7	1.9
	H50S50T180_3	61.2	-	-	-	0.87	-	-	-	-	62.3	4.8	0.8	0.0	32.1	1.9
	H50S50T180_u	61.5	-	-	-	0.84	-	-	-	-	60.9	4.4	0.3	0.0	34.4	1.8
	H100S0T180_u	41.1	-	-	-	1.8	-	-	-	-	65.6	4.4	0.0	0.0	30.0	2.2
After pyrolysis at 900°C	C0S100T	-	44.5	44.5	1416	471	0.20	0.19	0.38	0.32	90.4	0.8	0.6	0.0	8.2	11.0
	CH0S100T180_u	64.6	51.6	33.4	904	608	0.24	0.23	0.28	0.25	88.3	0.9	0.6	0.0	10.2	8.7
	CH50S50T180_1	63.0	50.4	31.8	1132	809	0.35	0.31	0.36	0.32	89.9	1.5	0.8	0.0	7.8	11.5
	CH50S50T180_2	60.0	53.2	31.9	1061	767	0.34	0.29	0.32	0.30	91.5	1.1	1.2	0.0	6.2	14.8
	CH50S50T180_3	61.2	48.4	29.6	984	643	0.27	0.25	0.29	0.27	90.8	2.1	0.8	0.0	6.3	14.4
	CH50S50T180_u	61.5	49.6	30.5	913	639	0.25	0.24	0.28	0.25	91.0	0.5	0.3	0.0	8.2	11.1
	CH100S0T180-u	41.1	51.2	21.1	836	562	0.22	0.22	0.26	0.23	93.0	0.5	0.1	0.0	6.4	14.5

219 A similar effect was found by decreasing the pH down to 2. Small spherical particles of  
220 around 2  $\mu\text{m}$  arranged in a necklace structure were indeed obtained in carbons based on either  
221 pure tannin (see Fig. 3d) or tannin-sucrose mixture (compare Fig. 3c, 3f, 3g and 3h) submitted  
222 to HTC at pH 2. No changes in particle diameter were observed, as their size was nearly  
223 constant around 2  $\mu\text{m}$ , irrespective to the HTC temperature: 160, 180 or 200°C. This finding  
224 at lower pH is different from what was formerly observed for HOS100T at unchanged pH and  
225 160°C, for which irregular spheres were found, indicating that HTC reaction was not finished.  
226 By increasing the HTC temperature from 180 to 200°C, bigger and rounded spheres were  
227 observed (Braghiroli et al., 2014).

228 Figs. 3b and 3e show SEM pictures of carbon materials derived from 100S0T submitted to  
229 HTC at unchanged pH (pH around 4) or at pH 2. HTC of 100S0T at unchanged pH produced  
230 mostly monodisperse spherical particles having a size of approximately 1  $\mu\text{m}$ , in agreement  
231 with other authors (Titirici et al., 2008; Sevilla and Fuertes, 2009). However, sucrose  
232 hydrolysis at pH 2 produced bigger spheres of around 5-10  $\mu\text{m}$ . Zhao et al. (2013) observed  
233 the effect of the acidic pH on the formation mechanism of carbon spheres when submitting  
234 cellulose to HTC. The compounds obtained from cellulose hydrolysis rapidly react with  $\text{H}^+$   
235 present in the system through dehydration and polymerisation reactions and lead to hydrochar  
236 nucleation. Besides that, they concluded that the acid concentration in the HTC system could  
237 also control the shape and the diameter of the carbon spheres.

238 Figure 3

239 Table S1 shows the main characteristics of hydrochars and carbon materials prepared with  
240 50% of sucrose (50S50T) at different HTC temperatures (160, 180 and 200°C) and different  
241 pH. Some of these results are summarised in Fig. 4 including the total carbon yield and the  
242  $A_{BET}$  as a function of HTC temperature at unchanged pH or at pH 2. The HTC yield was  
243 around 60% irrespective to the temperature or the pH. After pyrolysis, the total carbon yield

244 appears to be constant, around 30%, whatever the HTC temperature or the pH used  
245 beforehand. In the same way,  $A_{BET}$  did not change with HTC temperature but was higher for  
246 samples prepared at pH 2. Indeed, carbons prepared from hydrochars obtained at pH 2  
247 presented an  $A_{BET}$  of  $735 \pm 32 \text{ m}^2 \text{ g}^{-1}$ , while those prepared at unchanged pH had an  $A_{BET}$  of  
248  $629 \pm 10 \text{ m}^2 \text{ g}^{-1}$ .

249 Figure 4

250 In order to study the effect of the percentage of sucrose on the hydrochar characteristics,  
251 hydrochars based on various proportions of tannin and sucrose were prepared at unchanged  
252 pH and at pH 2, summarised in [Table S2](#). We can observe by SEM photos in [Fig. 5a to 5c](#)  
253 that, by increasing the weight fraction of sucrose from 25 to 100% at unchanged pH, the  
254 sphere diameter decreased from around 10 to 2  $\mu\text{m}$  and they became more individualised and  
255 more monodispersed. Polydispersity and higher particle size thus appear to be a consequence  
256 of tannin presence in the system at unchanged pH. In the literature, changes of particles  
257 morphology produced by mixing two carbon precursors submitted to HTC were also  
258 evidenced for microalgae in the presence of glucose added in a mass ratio of 1:1. In that case,  
259 the final particles morphology was that of pure glucose but with a double higher average  
260 diameter, passing from 1 to 2  $\mu\text{m}$  (Falco et al., 2012). Coming back to the present situation,  
261 the effect of adding sucrose at pH 2 was opposite to that observed at unchanged pH. With the  
262 addition of sucrose at lower pH, the average sphere diameter increased from 1-2  $\mu\text{m}$  to 2-3  
263  $\mu\text{m}$  and finally to around 5-10  $\mu\text{m}$  when the proportion of sucrose increased from 25% ([Fig.](#)  
264 [5d](#)), to 75% ([Fig. 5d](#)) until 100% ([Fig. 5f](#)), respectively.

265 Figure 5

266 [Fig. 6a](#) shows the HTC yield of all materials at different proportions of sucrose / tannin and  
267 at two pH, unchanged and 2. The dotted lines represent the theoretical yield calculated from

268 the experimental yields of 0S100T and 100S0T (e.g. for 75S25T we have  $Y_{HTC, 75S25T} = (75 \times$   
269  $Y_{HTC,100S0T} / 100 + 25 \times Y_{HTC,0S100T} / 100)$ , in order to observe any synergetic effect between  
270 tannin and sucrose during HTC. At pH 2, the experimental HTC yield was very similar to the  
271 expected value, so we can conclude that there is no apparent interaction between sucrose and  
272 tannin regarding the yield. Acidic pH accelerates HTC reactions, both for sucrose and tannin  
273 precursors (Lee et al., 1999; Kim et al., 2001; Trajano and Wyman, 2013) and no differences  
274 were observed. At unmodified pH, experimental HTC yield of tannin-sucrose mixtures were  
275 higher than those theoretically calculated, suggesting that HTC products of sucrose and tannin  
276 interact with each other. At pH around 4, sucrose yielded more solid materials. Its higher  
277 HTC kinetics compared to tannin led to more germs with a resulting lower particle size and an  
278 enhanced HTC yield. Since at pH 2 the experimental HTC yield was the same as calculated, it  
279 can be assumed that a low pH promotes fast reactions to liquid products (Lee et al., 1999;  
280 Kim et al., 2001; Trajano and Wyman, 2013) that do not interact with tannin.

281 Figure 6

### 282 3.2 Porous texture and composition

283 Fig 6b shows the BET area of the same hydrochars as in Fig. 6a but after pyrolysis at  
284 900°C. As a general remark, the addition of sucrose to tannin slightly increased  $A_{BET}$ . The  
285 highest  $A_{BET}$  was found for the mixture 50S50T at both pH, but the main effect on the increase  
286 of surface area was due to the pH reduction. Fig. 7 shows that the product  $A_{BET} \times$  total carbon  
287 yield increased with the total carbon yield. This effect is opposite to what is obviously found  
288 for carbon activation, whether physical or chemical, which produces higher surface area when  
289 the carbon yield decreases, i.e., when the burn-off increases. Besides, by increasing the  
290 proportion of tannin mixed with sucrose in HTC conditions, an increase of the total carbon  
291 yield can be seen. However, the highest  $A_{BET}$  was obtained at equal proportion (50:50) of T  
292 and S at pH 2. Such increase of surface area, from 476 to 791  $\text{m}^2 \text{g}^{-1}$ , cannot be explained by

293 the decrease of particle diameter from 10  $\mu\text{m}$  (CH0S100T180\_u) to approximately 2  $\mu\text{m}$   
294 (CH50S50T180\_2), which accounts for less than 1% of the measured  $A_{BET}$ . As previously  
295 discussed in Braghiroli et al. (2015b), the decrease of particle size might facilitate the  
296 evolution of volatile matter and then the development of textural properties.

297 Figure 7

298 All materials were found to be microporous, given their Type I nitrogen isotherms at -  
299 196°C, having a vertical part at low relative pressure  $P/P_0$  and an almost horizontal part from  
300  $P/P_0 = 0.02$  to 1 as shown in Fig. 8a for CH50S50T180\_2 and CH50S50T180\_u. The pore  
301 size distribution calculated by NLDFT is presented in Fig. 8b for the same samples;  
302 CH50S50T180\_2 had some porosity in the mesopore range (between 2 and 10 nm), whereas  
303 CH50S50T180\_u presented an entirely microporous structure. The isotherm of sample  
304 prepared at pH 2 presented a slight slope showing the presence of pores broader than 2 nm.  
305 Most of the carbohydrates submitted to HTC needed a second thermal treatment, at higher  
306 temperature, to increase the porosity of the resultant carbon materials. However, glucose after  
307 HTC and subsequent pyrolysis at 900°C was poorly porous and had low surface areas, around  
308 30-50  $\text{m}^2 \text{g}^{-1}$  (Zhao et al., 2010). Thanks to the reactivity of tannins in hydrothermal  
309 conditions and posterior pyrolysis at 900°C, highly porous material were obtained ( $A_{BET} > 600$   
310  $\text{m}^2 \text{g}^{-1}$ ) confirming its potential as precursor for the production of porous carbons.

311 Figure 8

312 As for the chemical composition, Fig. 9a shows the van Krevelen diagram for all  
313 hydrochars and carbon materials prepared from tannin and sucrose at different pH and HTC  
314 temperatures (160, 180 and 200°C). The main arrow (from 100S0T to HTC\_900°C, i.e., from  
315 pure sucrose to all carbons obtained by HTC followed by pyrolysis at 900°C) indicates the  
316 loss of oxygen and hydrogen, and therefore the increase of carbon content after both thermal  
317 treatments (HTC at 160-200°C and pyrolysis at 900°C) (van Krevelen, 1950). The percentage



318 of carbon increased after HTC and obviously even more after pyrolysis. After HTC, samples  
319 prepared at unmodified pH retained more oxygen, 30-36 wt. %, than those prepared at pH 2,  
320 28-33 wt. %. After pyrolysis at 900°C, carbon derived from hydrochars prepared at  
321 unmodified pH retained more oxygen, 6-10 wt. %, than those prepared at pH 2, 3-6 wt. %.

322 [Fig. 9b](#) shows the total amounts of CO and CO<sub>2</sub> gases in mmol g<sup>-1</sup> that have been lost  
323 during a thermal treatment (TPD analysis) up to 1100°C for materials at different T/S  
324 proportions. CO<sub>2</sub> derives from precursors comprising carboxylic acids, lactones and  
325 anhydride groups, and CO derives from quinonic and phenolic groups (Figueiredo et al.,  
326 1999). Boudouard equilibrium also takes place, modifying the CO/CO<sub>2</sub> ratio. The total  
327 amount of released gases (CO + CO<sub>2</sub>) was higher for materials HsStT\_u prepared without pH  
328 modification (0.065-0.075 mmol g<sup>-1</sup>) than for HsStT\_2 prepared at pH 2 (0.036-0.052 mmol  
329 g<sup>-1</sup>). This is in good agreement with their higher amount of oxygen, 32.4-36.3 wt. %,   
330 compared to 30.6-32.7 wt. % in HsStT\_2 materials, measured by EA ([Table 1](#) and [Table S1](#)).  
331 Indeed, tannin in the presence of strong acids undergoes dehydration and condensation  
332 reactions (Pizzi, 1983; Braghiroli et al., 2015a), which might have reduced the amount of  
333 oxygen in hydrochars.

#### 334 Figure 9

335 Surface atomic concentrations obtained by XPS and contributions to the C1s, O1s and N1s  
336 high-resolution spectra of the hydrochars and carbon materials are collected in [Table 2](#) and in  
337 [Fig. S1](#) to [S6](#) of the Supporting Information section. Tannin-derived hydrochars presented  
338 high oxygen surface concentrations, between 12.6 and 19.6 at. %, but low nitrogen surface  
339 concentrations, between 0.3 and 1.3 at. %. No influence of the pH of the medium on the  
340 oxygen surface concentration of the hydrochars was evidenced. Sucrose-derived hydrochars  
341 contained 17.9 at. % surface oxygen, and a small concentration of nitrogen, 0.3 at. %, in  
342 agreement with the chemical composition of sucrose and with the presence of amino-acids

343 coming from the raw sugar beet. As expected, the oxygen concentration of the hydrochars  
344 significantly decreased after pyrolysis, and the resultant carbons exhibited oxygen surface  
345 concentrations between 2.3 and 11.7 at. %. The concentration of nitrogen varied in the range  
346 0.40 – 1.7 at. %, being only present at the surface of carbons prepared at pH higher than 3.

347 Deconvolution of the high-resolution XPS spectra allowed identifying chemical bonds that  
348 are characteristic of specific functional groups. C1s high-resolution spectra for all samples  
349 exhibited an asymmetric peak centred on binding energies (BE) of 284.4 – 284.5 eV (Table 2,  
350 and Fig. S1 and S4 in the Supporting Information section). Except for H50S50T180\_3, the  
351 deconvolution of the C1s high-resolution profiles gave rise to five peaks, CI to CV, with  
352 binding energies (BE) between 284.4 and 290.6 eV: CI is assigned to Csp<sup>2</sup> in hydrocarbons,  
353 aromatics and aliphatics; CII is associated with Csp<sup>3</sup> and C-O single bonds associated with  
354 ethers, phenols and anhydrides; CIII is assigned to C=O double bonds in carbonyls and  
355 quinones; CIV corresponds to C-O single bonds in carboxylic groups; and CV is related to  
356 plasmon losses or shake-up  $\pi$ - $\pi$  satellites. In the case of H50S50T180\_3, an additional peak  
357 C\* appeared at an unusually low BE, 283.6 eV. This peak may be associated to pre-graphite-  
358 like C in highly aromatic materials (Cagniant et al., 1998; Weckhuysen et al., 1998).

359 The O1s high-resolution spectra of the hydrochars presented, in general, two oxygen  
360 contributions (Table 2): O1, assigned to C=O double bonds in quinone-type groups, carbonyls  
361 and carboxylic acids; and O2, related to –OH bonds in phenols, C–O–C in ether groups and  
362 C=O bonds in ester and anhydride groups. The O1s high-resolution spectra exhibited  
363 generally O1, O2 and O3 contributions, O3 being assigned to chemisorbed oxygen, single C-  
364 O bonds in esters and anhydrides, and C-O bonds in carboxylic groups and/or water.

365 Finally, the deconvolution of the N1s high-resolution spectra was only possible for  
366 samples with surface nitrogen concentrations higher than 1 at. %. Curve fitting was not  
367 possible for the N1s high-resolution spectrum of H50S50T180\_3 hydrochar, due to the low

368 area of the peak. N1s high-resolution spectra of both hydrochars and carbons exhibited three  
369 contributions assigned to three types of functional groups: N6, related to pyridinic nitrogen;  
370 N5, related to pyrrolic nitrogen; and NQ, assigned to quaternary nitrogen (Briggs, 2005;  
371 Dongil et al., 2011; Weidenthaler et al., 2006).

372 In general, pyrolysis decreased the relative concentrations of the groups related to CII and  
373 OII, while increasing the relative amounts of the groups related to the peaks CIII, CIV and OI.  
374 This finding means that the concentration of ethers, phenols, esters and anhydrides decreased  
375 whereas the concentration of quinone-type groups, carbonyls and carboxylic acids increased  
376 as a consequence of pyrolysis.

377 Concerning the structure of the carbons obtained by pyrolysis at 900°C of the  
378 aforementioned hydrochars, it can be added that none of these materials are graphitic, as  
379 evidenced by their XRD patterns showing very broad and poorly defined (002) and (10l)  
380 bands (see for instance (Tondi et al., 2009) and the supplementary information of (Celzard et  
381 al., 2019) for typical patterns of carbons based on tannin and tannin-sugar produced at  
382 900°C). The corresponding Raman spectra demonstrated the same, but also that these  
383 materials are not graphitisable either, unless transition metals are added as graphitisation  
384 catalyst, which was not the case here. Typical Raman spectra of carbons based on tannin and  
385 tannin-sugar produced at 900°C can be found elsewhere (Celzard et al., 2019; Braghiroli et  
386 al., 2017), and prove that the present materials are definitely highly disordered, i.e. very  
387 poorly crystallised, carbons.

388 Concerning the morphology, carbon spheres have a wide range of applications, depending  
389 on their diameter, pore texture and surface chemistry. For example, they can be used in  
390 batteries (Park et al., 2018) or supercapacitors (Zhou et al., 2015), as catalysts (Frusteri et al.,  
391 2016, Maciá- Agulló et al., 2010) or even as boosters to produce pure water as we reported  
392 recently (Celzard et al., 2019).

393 **Table 2.** Atomic surface concentrations of C, N and O, and contributions to the C1s, O1s and N1s high-resolution XPS spectra of the materials in  
 394 terms of peak area fraction (%) at given binding energies (BE, eV).

Sample name	Concentration (at. %)			C1s peak BE (eV) Area (%)						O1s peak BE (eV) Area (%)			N1s peak BE (eV) Area (%)			
	C	O	N	C*	CI	CII	CIII	CIV	CV	O1	O2	O3	N6	N5	NQ	NX
<b>OS100T</b>	80.4	19.6	-	-	284.4 66.1	285.8 29.6	288.2 2.5	289.2 0.9	291.0 0.9	531.7 24.8	532.8 75.2	-	-	-	-	-
<b>H50S50T180_1</b>	81.9	16.8	1.3	-	284.4 65.9	285.7 27.3	287.6 5.6	289.0 0.7	290.3 0.4	531.4 36.1	532.7 63.9	-	398.5 12.2	399.7 59.9	401.1 27.9	-
<b>H50S50T180_2</b>	83.0	15.7	1.3	-	284.4 73.7	285.8 19.4	287.6 4.6	288.9 1.9	290.6 0.4	531.4 41.7	532.7 58.3	-	398.5 28.1	399.7 58.5	401.1 13.4	-
<b>H50S50T180_3</b>	87.1	12.6	0.3	283.6 9.0	284.5 31.4	286.0 44.3	287.6 12.2	289.0 1.0	290.1 2.1	531.8 7.2	533.3 60.8	534.5 32.0	-	-	-	-
<b>H50S50T180_u</b>	84.2	15.8	-	-	284.4 73.7	285.7 20.7	287.6 3.7	289.0 1.6	290.3 0.3	531.7 39.5	532.8 60.5	-	-	-	-	-
<b>H100S0T180_u</b>	81.9	17.9	0.3	-	284.4 65.4	285.6 25.8	287.6 8.1	289.2 0.3	290.4 0.4	531.5 40.1	532.8 59.9	-	-	-	-	-
<b>C0S100T</b>	97.1	2.9	-	-	284.4 66.4	285.5 25.5	287.6 5.7	289.2 1.8	290.5 1.5	531.8 40.4	533.0 54.0	534.5 5.6	-	-	-	-
<b>CH50S50T180_1</b>	97.5	2.5	-	-	284.5 68.7	285.5 23.8	287.6 5.2	289.2 1.4	290.4 1.5	531.6 48.1	532.9 49.4	534.5 2.5	-	-	-	-
<b>CH50S50T180_2</b>	97.2	2.8	-	-	284.5 65.8	285.5 25.8	287.6 5.6	289.0 0.6	290.2 2.2	531.6 41.4	532.9 47.0	534.5 11.9	-	-	-	-
<b>CH50S50T180_3</b>	94.8	3.4	1.7	-	284.4 66.2	285.5 25.3	287.6 5.9	289.2 1.1	290.4 1.5	531.3 46.5	532.8 51.0	534.5 2.5	398.2 28.8	400.3 32.7	401.1 38.5	-
<b>CH50S50T180_u</b>	87.9	11.7	0.40	-	284.4 75.9	286.0 19.5	287.6 3.2	289.2 0.7	290.1 0.4	531.9 53.3	533.2 46.7	-	-	-	-	-
<b>CH100S0T180_u</b>	97.7	2.3	-	-	284.5 67.1	285.6 25.4	287.7 4.8	289.2 0.6	290.4 2.1	532.0 49.2	533.0 47.8	534.5 3.0	-	-	-	-

395

### 396 3.3 Electrochemical properties

397 Among the carbon materials, C0S100T, CH50S50T180\_1 and CH50S50T180\_u were  
398 selected for studying their electrochemical behaviour. With respect to porous texture,  
399 C0S100T and CH50S50T180\_1 are among the materials having the highest micropore  
400 volumes, although their PSDs are clearly not the same, as suggested by the data of Table 1.  
401 With respect to surface chemistry, the most remarkable difference in their surface chemistry is  
402 that CH50S50T180\_u exhibited higher surface oxygen content than the other two carbons,  
403 and that CH50S50T180\_1 exhibited higher relative concentrations of quinone and carbonyl  
404 groups (OI peak). The latter are the most electroactive oxygen functionalities in acidic  
405 electrolytes (Inagaki et al., 2010). Choosing such materials for electrochemical tests was  
406 therefore supposed to clarify the understanding of these new carbon materials.

407 At the lowest scan rate of  $0.5 \text{ mV s}^{-1}$ , cyclic voltammetry (CV) curves of C0S100T and  
408 CH50S50T180\_1 exhibited more defined peaks of both anodic and cathodic currents than  
409 CH50S50T180\_u despite possessing a lower concentration of oxygen on their surfaces (Fig.  
410 10a). The presence of redox peaks is due to a contribution of the surface oxygen groups to the  
411 total capacitance of the electrodes by a pseudocapitance mechanism. Even at this low scan  
412 rate of  $0.5 \text{ mV s}^{-1}$ , CV curves of CH50S50T180\_u exhibited a highly distorted profile with  
413 respect to the rectangular shape of an ideal electric-double layer capacitor (ELDC). This fact  
414 may indicate the existence of kinetic limitations for ion transport, and agrees with the highly  
415 microporous texture of the carbon, whose percentage of narrow porosity (width  $< 0.7 \text{ nm}$ ) was  
416 the highest of the three materials, 84.0%, and whose percentage of mesoporosity was the  
417 lowest one, 0.0%. At the relatively low scan rate of  $10 \text{ mV s}^{-1}$ , the shape of the CV curves of  
418 all the materials clearly deviated from the rectangular one, and no clear peak could be seen  
419 (Fig. 10b). This suggests that the behaviour of the supercapacitor electrodes becomes less

420 capacitive and more resistive, due to kinetic limitations, and that pseudocapacitance  
421 contribution is negligible, respectively (McDonough et al., 2012).

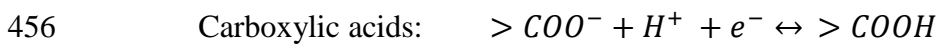
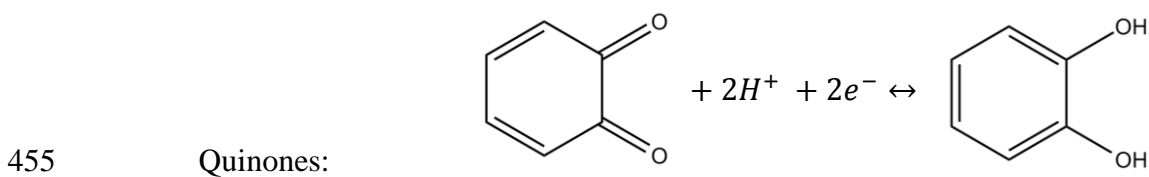
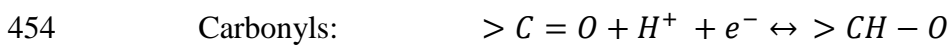
422 The studied electrode materials yielded similar values of specific capacitance in the entire  
423 range of investigated scan rates. At the lowest scan rate of  $0.5 \text{ mV s}^{-1}$ , specific capacitances of  
424 51, 57 and  $58 \text{ F g}^{-1}$  were exhibited by C0S100T, CH50S50T180\_1 and CH50S50T180\_u,  
425 respectively (Fig. 10c). These capacitance values progressively decreased when the scan rate  
426 increased, due to the increasing resistance to diffusion of electrolyte ions into the pores. At  
427  $100 \text{ mV s}^{-1}$  scan rate, the specific capacitance was  $15 \text{ F g}^{-1}$  for all the materials (Fig. 10c),  
428 which corresponds to capacitance retentions of 30.4, 26.6 and 26.3% for C0S100T,  
429 CH50S50T180\_1 and CH50S50T180\_u, respectively (Fig. 10d). The lower capacitance  
430 retention of CH50S50T180\_1 and CH50S50T180\_u compared to C0S100T indicates the  
431 existence of more important kinetic limitations at increasing scan rates due to their high  
432 fractions of narrow porosity, 71.4 and 84.0%, respectively. The CV results agree with a  
433 previous study on molasses-derived carbons, in which the materials prepared by HTC  
434 exhibited, in the studied potential window, lower capacitances than those that were directly  
435 pyrolysed, mainly due to their narrow porosities and low electrical conductivities (Sanchez-  
436 Sanchez et al., 2016).

437 Figure 10

438 In order to determine the pseudocapacitance contribution to the overall capacitance of the  
439 materials, interfacial capacitances at different scan rates,  $C / S_{NLDFT}$ , were plotted versus  
440 oxygen surface concentrations (Fig. S7a of the Supporting Information section). The  
441 interfacial capacitance was calculated by considering  $S_{NLDFT}$  instead of  $A_{BET}$ , since it has been  
442 previously shown that this approach is more appropriate for materials mainly comprising  
443 narrow pores, such as in the present case (Sanchez-Sanchez et al., 2016). In general, higher  
444 surface oxygen concentrations were not related to higher interfacial capacitances in the entire

445 range of studied scan rates. This should mean that the pseudocapacitance contribution of the  
 446 materials is lower than the capacitive contribution, for which the porous texture is the key  
 447 parameter.

448 Oxygen functional groups have a great influence on the electrochemical properties of  
 449 carbon materials (Anjos et al., 2013; Tanaka et al., 2015). Hydroxyl, carbonyl and, especially,  
 450 quinone groups, have been proved to yield more capacitance than carboxyl, anhydride or  
 451 lactone groups in acidic aqueous electrolytes thanks to their Faradaic reactions (Inagaki et al.,  
 452 2010). Redox reactions involving these groups are the following (Oh et al., 2014):



457 where the symbol > represents the surface of the carbon material. Protons,  $H^+$ , are not only  
 458 simply adsorbed on the oxygen functional groups, but are involved in the electrochemical  
 459 reactions.

460 As a consequence of these Faradaic reactions, redox peaks can appear on the anodic and  
 461 cathodic branches of the CV curves of the carbon materials. CV curves obtained in a three-  
 462 electrode cell in  $1 \text{ mol L}^{-1} \text{ H}_2\text{SO}_4$  electrolyte, measured at  $0.5 \text{ mV s}^{-1}$  scan rate and  
 463 considering the first cycle of cycling, are displayed in Fig. 11. These curves exhibited two  
 464 redox processes associated to peaks 1 and 2 appearing in the anodic and cathodic branches,  
 465 which are represented by the “ox” and “red” superscript, and are defined by two parameters:

466 (i) peak current,  $I_p$ , which is the current at the maximum of the peak; and (ii) peak potential,  
467  $E_p$ , which is the potential at the maximum of the peak (Fig. 11a, 11c and 11e).

468 Figure 11

469 For the samples C0S100T and CH50S50T180\_1, no second anodic peak,  $I_{p,2}^{ox}$ , was seen,  
470 indicating the irreversibility of the associated redox process. In contrast, the first peak could  
471 be clearly observed both in the anodic and cathodic branches and appeared in the five cycles  
472 studied at scan rates from 0.5 to 5  $\text{mV s}^{-1}$  for C0S100T, and from 0.5 to 2  $\text{mV s}^{-1}$  for  
473 CH50S50T180\_1 and CH50S50T180\_u. This suggests that the associated redox system may  
474 be quasi-reversible in the aforementioned scan rate intervals. The highly distorted CV curves  
475 with respect to the expected rectangular shape of an ideal electric-double layer capacitor at  
476 scan rates above 2 or 5  $\text{mV s}^{-1}$  did not allow differentiating clear redox peaks. Therefore, the  
477 reversibility of the redox system 1 was studied up to a maximum scan rate of 5  $\text{mV s}^{-1}$ . The  
478 formal potentials of peak 1 vs SCE reference, calculated as  $E^0 = 1/2 (E_{p,1}^{ox} + E_{p,1}^{red})$ , were  
479 0.425, 0.424 and 0.444 V for C0S100T, CH50S50T180\_1 and CH50S50T180\_u,  
480 respectively. The reversible character of the redox process was evaluated through the  
481 following criteria:

482 1) *Peak separation*,  $\Delta E = E_{p,1}^{ox} - E_{p,1}^{red} \leq 0.059 / n$ , where  $E_{p,1}^{ox}$  and  $E_{p,1}^{red}$  (V) are the  
483 maxima of the anodic and cathodic peaks, respectively, and  $n$  is the number of transferred  
484 electrons: Considering the transfer of 1 electron, the peak separation was lower than 0.059 V  
485 at the lowest scan rate of 0.5  $\text{mV s}^{-1}$  for the three materials, suggesting the reversibility of the  
486 redox process.  $\Delta E$  generally increased above 0.059 V as the cycle number increased, which  
487 indicates that the redox process was progressively less reversible due to the gradual  
488 transformation of surface groups into non-electroactive species. However,  $\Delta E$  was  
489 progressively lower than 0.059 V at the scan rate of 0.5  $\text{mV s}^{-1}$  for the sample C0S100T,  
490 suggesting a higher reversibility of the redox process (Fig. 11b, 11d and 11f). This can be



491 explained by the improvement of the surface wettability during the cycling process, which  
492 facilitates the contact between the surface functionalities and the electrolyte ions, so that  
493 redox reactions are easier to occur, and also by the higher fraction of pores involved in the  
494 materials as the cycling process goes on (Jiang et al., 2013). Varying the scan rate in cyclic  
495 voltammetry allows varying the diffusion layer thickness, thus enabling the control of the  
496 electrochemical process either by electron transfer or by mass transport. The diffusion layer is  
497 thicker at low scan rates, and thinner as the scan rate increases. Electrochemical processes  
498 reflect the competition between reactions at the electrodes and diffusion, so that faster scan  
499 rates favour electrochemical irreversibility, which is controlled by the electron transfer rate,  
500 and the peak potentials are thus shifted. This trend is clearly observed in Fig. S7b of the  
501 Supporting Information section, which shows the progressive separation of maxima of the  
502 peaks associated to the redox process 1 at increasing scan rates from 0.5 to 2 mV s<sup>-1</sup> for a  
503 representative sample, COS100T (McDonough et al., 2012). When the peak potentials remain  
504 constant with increasing scan rates, the involved redox process is reversible. Fig. 12b, 12d and  
505 12f show the progressive increase of the peak potentials of the studied samples,  $E_p^{ox,red}$ , at  
506 increasing scan rates,  $\ln s$ , indicating the quasi-reversibility of the involved redox system  
507 (Gómez et al., 2011).

508 2) *Ratio of anodic to cathodic currents,  $I_{p,1}^{ox} / I_{p,1}^{red} \approx 1$ , where  $I_{p,1}^{ox}$  and  $I_{p,1}^{red}$  (A) are the*  
509 *currents at the maximum of the anodic and cathodic peaks, respectively:* When the peak  
510 currents,  $I_p$ , for the oxidation and reduction reactions are the same, i.e.,  $I_{p,1}^{ox} / I_{p,1}^{red} = 1$ , the  
511 redox process is reversible (Bard and Faulkner, 2001). The current ratios of the studied  
512 samples at scan rates ranging from 0.5 to 2 mV s<sup>-1</sup> were  $0.98 \pm 0.04$ , which indicates the  
513 quasi-reversibility of the redox process.

514 3) *Scan rate dependence of peak current,  $I_p^{ox,red} \propto s^{1/2}$ , where  $I_p^{ox,red}$  (A) is the current at*  
515 *the maximum of the anodic or the cathodic peaks and  $s^{1/2}$  (V<sup>1/2</sup> s<sup>-1/2</sup>) is the square root of the*

516 *scan rate*: A linear relationship between  $I_p^{ox,red}$  and  $s^{1/2}$  indicates that the redox process is  
517 quasi-reversible (Gómez et al., 2011) As shown in Fig. 12a, 12b and 12c,  $I_p^{ox,red}$  versus  $s^{1/2}$   
518 leads to linear relationships for the studied samples, with determination coefficients close to 1,  
519 thus indicating that the concerned redox processes are quasi-reversible. From these linear  
520 relationships and applying the Randles-Sevcik equation (Eq. 2), the diffusion coefficients,  $D_0$ ,  
521 of the processes were calculated (McDonough et al., 2012). The Randles-Sevcik equation  
522 reads:

$$523 \quad I_p = 0.4463 n F A C [(F D_0 s) / (R T)]^{1/2} \quad (2)$$

524 where  $I_p$  (A) is the peak current,  $n$  is the number of electrons transferred in the reaction,  $F$  (C  
525 mol<sup>-1</sup>) is the Faraday constant,  $A$  (cm<sup>2</sup>) is the electrode area,  $C$  (mol L<sup>-1</sup>) is the concentration  
526 of the diffusing species in the bulk of the electrolyte,  $D_0$  (cm<sup>2</sup> s<sup>-1</sup>) is the corresponding  
527 diffusion coefficient,  $s$  (V s<sup>-1</sup>) is the scan rate,  $R$  (J mol<sup>-1</sup> K<sup>-1</sup>) is the universal gas constant and  
528  $T$  (K) is the temperature. Considering that  $n = 1$  and  $C = 1$  mol L<sup>-1</sup> (H<sub>2</sub>SO<sub>4</sub>), the diffusion  
529 coefficients were found to be  $1.602 \times 10^{-13}$ ,  $1.156 \times 10^{-13}$  and  $6.973 \times 10^{-14}$  cm<sup>2</sup> s<sup>-1</sup> for  
530 C0S100T, C50S50T180\_1 and C50S50T180\_u, respectively. These values are considerably  
531 lower than those obtained for well-established redox processes in other doped carbons used as  
532 electrode materials, such as graphene-polyaniline (PANI) nanocomposites or PANI systems  
533 alone, suggesting a hindered ion transport (Gómez et al., 2011). Therefore, activation for  
534 opening the porosity and developing it further appears necessary for improving the  
535 electrochemical performance of these materials. For instance, we have recently shown that  
536 CO<sub>2</sub> activation allows increasing the surface area of tannin-derived mesoporous carbons up to  
537 nearly 2000 m<sup>2</sup>/g and maintaining high-rate capability when increasing the current density up  
538 to 80 A/g (Castro-Gutiérrez et al., 2019). The same kind of behaviour can therefore be  
539 expected with the present samples.

540

Figure 12

#### 541 **4. Conclusions**

542 Tannin-sucrose blends mixed in various proportions were submitted to hydrothermal  
543 carbonisation (HTC) at different pH and temperatures, and then pyrolysed at 900°C under  
544 nitrogen flow. Microporous carbon spheres with BET areas as high as 810 m<sup>2</sup>/g, without  
545 further activation, were produced. Adding more sucrose produced microspheres of lower  
546 particle size due to the increased amount of germs produced by the HTC of sucrose.

547 HTC was confirmed to be an interesting low-cost and environment-friendly step to tune the  
548 properties of the resultant carbon materials, modifying their porous texture and their chemical  
549 composition, and thus broadening the range of their properties and therefore of their  
550 applications. The preliminary electrochemical tests reported here were carried out to select the  
551 most promising materials for further research. Although the carbon electrodes presented a  
552 quasi-reversible redox reaction concerning oxygen groups, their narrow pores hindered  
553 transport of electrolyte ions and led to low values of capacitance retention when increasing  
554 the current density and the scanning rate. Activation should significantly improve this results,  
555 and will be the object of a forthcoming study.

556

#### 557 **Acknowledgements**

558 The present research was partly made possible by the support of the Region Lorraine and  
559 University of Lorraine through the programme ‘Jeunes chercheurs’. The French authors also  
560 gratefully acknowledge the financial support of the CPER 2007-2013 “Structuration du Pôle  
561 de Compétitivité Fibres Grand’Est” (Competitiveness Fibre Cluster), through local (Conseil  
562 Général des Vosges), regional (Région Lorraine), national (DRRT and FNADT) and  
563 European (FEDER) funds.

- 565 Anjos, D.M., McDonough, J.K., Perre, E., Brown, G.M., Overbury, S.H., Gogotsi, Y.,  
566 Presser, V., 2013. Pseudocapacitance and performance stability of quinone-coated  
567 carbon onions. *Nano Energy* 2, 702–712.  
568 <https://doi.org/10.1016/j.nanoen.2013.08.003>
- 569 Antal, M.J., Mok, W.S.L., Richards, G.N., 1990. Mechanism of formation of 5-  
570 (hydroxymethyl)-2-furaldehyde from d-fructose and sucrose. *Carbohydr. Res.* 199,  
571 91–109. [https://doi.org/10.1016/0008-6215\(90\)84096-D](https://doi.org/10.1016/0008-6215(90)84096-D)
- 572 Antonietti, M., Titirici, M.-M., 2010. Coal from carbohydrates: The “chimie douce” of  
573 carbon. *Comptes Rendus Chim.* 13, 167–173.  
574 <https://doi.org/10.1016/j.crci.2009.02.005>
- 575 Asghari, F.S., Yoshida, H., 2006. Acid-catalyzed production of 5-hydroxymethyl furfural  
576 from d-fructose in subcritical water. *Ind. Eng. Chem. Res.* 45, 2163–2173.  
577 <https://doi.org/10.1021/ie051088y>
- 578 Bard, A.J., Faulkner, L.R., 2001. *Electrochemical methods: fundamentals and applications*,  
579 2nd ed. ed. Wiley, New York.
- 580 Bate-Smith, E.C., 1962. The phenolic constituents of plants and their taxonomic significance.  
581 I. Dicotyledons. *J. Linn. Soc. Lond. Bot.* 58, 95–173. [https://doi.org/10.1111/j.1095-](https://doi.org/10.1111/j.1095-8339.1962.tb00890.x)  
582 [8339.1962.tb00890.x](https://doi.org/10.1111/j.1095-8339.1962.tb00890.x)
- 583 Braghiroli, F.L., Fierro, V., Izquierdo, M.T., Parmentier, J., Pizzi, A., Celzard, A., 2014.  
584 Kinetics of the hydrothermal treatment of tannin for producing carbonaceous  
585 microspheres. *Bioresour. Technol.* 151, 271–277.  
586 <https://doi.org/10.1016/j.biortech.2013.10.045>
- 587 Braghiroli, F.L., Fierro, V., Izquierdo, M.T., Parmentier, J., Pizzi, A., Celzard, A., 2012.  
588 Nitrogen-doped carbon materials produced from hydrothermally treated tannin.  
589 *Carbon* 50, 5411–5420. <https://doi.org/10.1016/j.carbon.2012.07.027>
- 590 Braghiroli, F.L., Fierro, V., Izquierdo, M.T., Parmentier, J., Pizzi, A., Delmotte, L., Fioux, P.,  
591 Celzard, A., 2015a. High surface – highly N-doped carbons from hydrothermally  
592 treated tannin. *Ind. Crops Prod.* 66, 282–290.  
593 <https://doi.org/10.1016/j.indcrop.2014.11.022>
- 594 Braghiroli, F.L., Fierro, V., Parmentier, J., Vidal, L., Gadonneix, P., Celzard, A., 2015b.  
595 Hydrothermal carbons produced from tannin by modification of the reaction medium:  
596 Addition of H<sup>+</sup> and Ag<sup>+</sup>. *Ind. Crops Prod.* 77, 364–374.  
597 <https://doi.org/10.1016/j.indcrop.2015.09.010>
- 598 Braghiroli, F.L., Fierro, V., Szczurek, A., Gadonneix, P., Ghanbaja, J., Parmentier, J.,  
599 Medjahdi, G., Celzard, A., 2017. Hydrothermal Treatment of Tannin: A Route to  
600 Porous Metal Oxides and Metal/Carbon Hybrid Materials. *Inorganics* 5, 7.  
601 <https://doi.org/10.3390/inorganics5010007>
- 602 Briggs, D., 2005. *Surface analysis of polymers by XPS and static SIMS*, Cambridge solid  
603 state science series. Cambridge University Press, Cambridge ; New York.
- 604 Cagniant, D., Gruber, R., Boudou, J.P., Bilem, C., Bimer, J., Salbut, P.D., 1998. Structural  
605 characterization of nitrogen-enriched coals. *Energy Fuels* 12, 672–681.  
606 <https://doi.org/10.1021/ef9700801>
- 607 Castro-Gutiérrez, J., Diez, N., Sevilla, M., Izquierdo, M.T., Ghanbaja, J., Celzard, A., Fierro,  
608 V., 2019. High-Rate Capability of Supercapacitors Based on Tannin-Derived Ordered  
609 Mesoporous Carbons. *ACS Sustainable Chem. Eng.* 7, 17627–17635.  
610 <https://doi.org/10.1021/acssuschemeng.9b03407>

611 Celzard, A., Fierro, V., Amaral-Labat, G., Szczurek, A., Braghiroli, F.L., Parmentier, J., Pizzi,  
612 A., Grishechko, L.I., Kuznetsov, B.N., 2012. Carbon gels derived from natural  
613 resources. *Bol. Grupo Esp. Carbón* 26, 2–7.

614 Celzard, A., Pasc, A., Schaefer, S., Mandel, K., Ballweg, T., Li, S., Medjahdi, G., Nicolas, V.,  
615 Fierro, V., 2019. Floating hollow carbon spheres for improved solar evaporation.  
616 *Carbon* 146, 232–247. <https://doi.org/10.1016/j.carbon.2019.01.101>

617 Dongil, A.B., Bachiller-Baeza, B., Guerrero-Ruiz, A., Rodríguez-Ramos, I., Martínez-Alonso,  
618 A., Tascón, J.M.D., 2011. Surface chemical modifications induced on high surface  
619 area graphite and carbon nanofibers using different oxidation and functionalization  
620 treatments. *J. Colloid Interface Sci.* 355, 179–189.  
621 <https://doi.org/10.1016/j.jcis.2010.11.066>

622 Falco, C., Sevilla, M., White, R.J., Rothe, R., Titirici, M.-M., 2012. Renewable nitrogen-  
623 doped hydrothermal carbons derived from microalgae. *ChemSusChem* 5, 1834–1840.  
624 <https://doi.org/10.1002/cssc.201200022>

625 Figueiredo, J.L., Pereira, M.F.R., Freitas, M.M.A., Órfão, J.J.M., 1999. Modification of the  
626 surface chemistry of activated carbons. *Carbon* 37, 1379–1389.  
627 [https://doi.org/10.1016/S0008-6223\(98\)00333-9](https://doi.org/10.1016/S0008-6223(98)00333-9)

628 Gómez, H., Ram, M.K., Alvi, Farah., Villalba, P., Stefanakos, E. (Lee), Kumar, A., 2011.  
629 Graphene-conducting polymer nanocomposite as novel electrode for supercapacitors.  
630 *J. Power Sources* 196, 4102–4108. <https://doi.org/10.1016/j.jpowsour.2010.11.002>

631 Frusteri, L., Cannilla, C., Bonura, G., Chuvilin, A.L., Perathoner, S., Centi, G., Frusteri, F.,  
632 2016. Carbon microspheres preparation, graphitization and surface functionalization  
633 for glycerol etherification. *Catal. Today* 277, 66–77.  
634 <https://doi.org/10.1016/j.cattod.2016.02.044>

635 Hemingway, R.W., Karchesy, J.J., Branham, S.J. (Eds.), 1989. *Chemistry and Significance of*  
636 *Condensed Tannins*. Springer US, Boston, MA. [https://doi.org/10.1007/978-1-4684-](https://doi.org/10.1007/978-1-4684-7511-1)  
637 [7511-1](https://doi.org/10.1007/978-1-4684-7511-1)

638 Hu, B., Wang, K., Wu, L., Yu, S.-H., Antonietti, M., Titirici, M.-M., 2010. Engineering  
639 carbon materials from the hydrothermal carbonization process of biomass. *Adv.*  
640 *Mater.* 22, 813–828. <https://doi.org/10.1002/adma.200902812>

641 Inagaki, M., Konno, H., Tanaike, O., 2010. Carbon materials for electrochemical capacitors.  
642 *J. Power Sources* 195, 7880–7903. <https://doi.org/10.1016/j.jpowsour.2010.06.036>

643 Jiang, J., Zhang, L., Wang, X., Holm, N., Rajagopalan, K., Chen, F., Ma, S., 2013. Highly  
644 ordered macroporous woody biochar with ultra-high carbon content as supercapacitor  
645 electrodes. *Electrochimica Acta* 113, 481–489.  
646 <https://doi.org/10.1016/j.electacta.2013.09.121>

647 Kabyemela, B.M., Adschiri, T., Malaluan, R.M., Arai, K., 1997. Kinetics of glucose  
648 epimerization and decomposition in subcritical and supercritical water. *Ind. Eng.*  
649 *Chem. Res.* 36, 1552–1558. <https://doi.org/10.1021/ie960250h>

650 Kim, J.S., Lee, Y.Y., Torget, R.W., 2001. Cellulose hydrolysis under extremely low sulfuric  
651 acid and high-temperature conditions. *Appl. Biochem. Biotechnol.* 91–93, 331–340.

652 Lee, Y.Y., Iyer, Prashant, Torget, R.W., 1999. Dilute-Acid Hydrolysis of Lignocellulosic  
653 Biomass, in: Tsao, G.T., Brainard, A.P., Bungay, H.R., Cao, N.J., Cen, P., Chen, Z.,  
654 Du, J., Foody, B., Gong, C.S., Hall, P., Ho, N.W.Y., Irwin, D.C., Iyer, P., Jeffries,  
655 T.W., Ladisch, C.M., Ladisch, M.R., Lee, Y.Y., Mosier, N.S., Mühlemann, H.M.,  
656 Sedlak, M., Shi, N.-Q., Tsao, G.T., Tolan, J.S., Torget, R.W., Wilson, D.B., Xia, L.  
657 (Eds.), *Recent Progress in Bioconversion of Lignocellulosics*. Springer Berlin  
658 Heidelberg, Berlin, Heidelberg, pp. 93–115. [https://doi.org/10.1007/3-540-49194-5\\_5](https://doi.org/10.1007/3-540-49194-5_5)

659 Letellier, M., Szczurek, A., Basso, M.-C., Pizzi, A., Fierro, V., Ferry, O., Celzard, A., 2017.  
660 Preparation and structural characterisation of model cellular vitreous carbon foams.  
661 Carbon 112, 208–218. <https://doi.org/10.1016/j.carbon.2016.11.017>  
662 Luijkx, G.C., van Rantwijk, F., van Bekkum, H., Antal, M.J., 1995. The role of deoxyhexonic  
663 acids in the hydrothermal decarboxylation of carbohydrates. Carbohydr. Res. 272,  
664 191–202.  
665 Maciá-Agulló, J.A., Sevilla, M., Diez, M.A., Fuertes, A.B., 2010. Synthesis of Carbon- based  
666 Solid Acid Microspheres and Their Application to the Production of Biodiesel.  
667 ChemSusChem 3, 1352-1354. <https://doi.org/10.1002/cssc.201000308>  
668 McDonough, J.K., Frolov, A.I., Presser, V., Niu, J., Miller, C.H., Ubieta, T., Fedorov, M.V.,  
669 Gogotsi, Y., 2012. Influence of the structure of carbon onions on their electrochemical  
670 performance in supercapacitor electrodes. Carbon 50, 3298–3309.  
671 <https://doi.org/10.1016/j.carbon.2011.12.022>  
672 Oh, Y.J., Yoo, J.J., Kim, Y.I., Yoon, J.K., Yoon, H.N., Kim, J.-H., Park, S.B., 2014. Oxygen  
673 functional groups and electrochemical capacitive behavior of incompletely reduced  
674 graphene oxides as a thin-film electrode of supercapacitor. Electrochimica Acta 116,  
675 118–128. <https://doi.org/10.1016/j.electacta.2013.11.040>  
676 Park, G.D., Kim, J.H., Lee, J.K., Kang, Y.C., 2018. Carbon microspheres with well-developed  
677 micro- and mesopores as excellent selenium host materials for lithium–selenium  
678 batteries with superior performances. J Mat Chem A 6, 21410-21418.  
679 <https://doi.org/10.1039/C8TA08727J>  
680 Pizzi, A., 1994. Advanced wood adhesives technology. M. Dekker, New York.  
681 Pizzi, A., 1983. Tannin-based wood adhesives, in: Pizzi, A. (Ed.), Wood Adhesives:  
682 Chemistry and Technology. Marcel Dekker, New York, pp. 177–246.  
683 Sanchez-Sanchez, A., Izquierdo, M.T., Medjahdi, G., Ghanbaja, J., Celzard, A., Fierro, V.,  
684 2018. Ordered mesoporous carbons obtained by soft-templating of tannin in mild  
685 conditions. Microporous Mesoporous Mater. 270, 127–139.  
686 <https://doi.org/10.1016/j.micromeso.2018.05.017>  
687 Sanchez-Sanchez, A., Martinez de Yuso, A., Braghiroli, F.L., Izquierdo, M.T., Alvarez, E.D.,  
688 Pérez-Cappe, E., Mosqueda, Y., Fierro, V., Celzard, A., 2016. Sugarcane molasses as  
689 a pseudocapacitive material for supercapacitors. RSC Adv 6, 88826–88836.  
690 <https://doi.org/10.1039/C6RA16314A>  
691 Schaefer, S., Fierro, V., Izquierdo, M.T., Celzard, A., 2016. Assessment of hydrogen storage  
692 in activated carbons produced from hydrothermally treated organic materials. Int. J.  
693 Hydrog. Energy 41, 12146–12156. <https://doi.org/10.1016/j.ijhydene.2016.05.086>  
694 Sevilla, M., Fuertes, A.B., 2009. Chemical and structural properties of carbonaceous products  
695 obtained by hydrothermal carbonization of saccharides. Chem. - Eur. J. 15, 4195–  
696 4203. <https://doi.org/10.1002/chem.200802097>  
697 Szczurek, A., Amaral-Labat, G., Fierro, V., Pizzi, A., Celzard, A., 2011a. The use of tannin to  
698 prepare carbon gels. Part II. Carbon cryogels. Carbon 49, 2785–2794.  
699 <https://doi.org/10.1016/j.carbon.2011.03.005>  
700 Szczurek, A., Amaral-Labat, G., Fierro, V., Pizzi, A., Masson, E., Celzard, A., 2011b. The use  
701 of tannin to prepare carbon gels. Part I: Carbon aerogels. Carbon 49, 2773–2784.  
702 <https://doi.org/10.1016/j.carbon.2011.03.007>  
703 Tanaka, S., Fujimoto, H., Denayer, J.F.M., Miyamoto, M., Oumi, Y., Miyake, Y., 2015.  
704 Surface modification of soft-templated ordered mesoporous carbon for  
705 electrochemical supercapacitors. Microporous Mesoporous Mater. 217, 141–149.  
706 <https://doi.org/10.1016/j.micromeso.2015.06.017>  
707 Tellez-Juárez, M.C., Fierro, V., Zhao, W., Fernández-Huerta, N., Izquierdo, M.T., Reguera,  
708 E., Celzard, A., 2014. Hydrogen storage in activated carbons produced from coals of

709 different ranks: Effect of oxygen content. *Int. J. Hydrog. Energy* 39, 4996–5002.  
710 <https://doi.org/10.1016/j.ijhydene.2014.01.071>

711 Titirici, M.-M., Antonietti, M., Baccile, N., 2008. Hydrothermal carbon from biomass: a  
712 comparison of the local structure from poly- to monosaccharides and  
713 pentoses/hexoses. *Green Chem.* 10, 1204. <https://doi.org/10.1039/b807009a>

714 Titirici, M.M., Thomas, A., Yu, S.-H., Müller, J.-O., Antonietti, M., 2007. A direct synthesis  
715 of mesoporous carbons with bicontinuous pore morphology from crude plant material  
716 by hydrothermal carbonization. *Chem. Mater.* 19, 4205–4212.  
717 <https://doi.org/10.1021/cm0707408>

718 Tondi, G., Zhao, W., Pizzi, A., Du, G., Fierro, V., Celzard, A., 2009. Tannin-based rigid  
719 foams: A survey of chemical and physical properties. *Bioresour. Technol.* 100, 5162–  
720 5169. <https://doi.org/10.1016/j.biortech.2009.05.055>

721 Trajano, H.L., Wyman, C.E., 2013. Fundamentals of Biomass Pretreatment at Low pH, in:  
722 Wyman, C.E. (Ed.), *Aqueous Pretreatment of Plant Biomass for Biological and*  
723 *Chemical Conversion to Fuels and Chemicals*. John Wiley & Sons, Ltd, Chichester,  
724 UK, pp. 103–128. <https://doi.org/10.1002/9780470975831.ch6>

725 Ulbricht, R., 1984. A review of 5-hydroxymethylfurfural (HMF) in parenteral solutions.  
726 *Fundam. Appl. Toxicol.* 4, 843–853. [https://doi.org/10.1016/0272-0590\(84\)90106-4](https://doi.org/10.1016/0272-0590(84)90106-4)

727 Unur, E., 2013. Functional nanoporous carbons from hydrothermally treated biomass for  
728 environmental purification. *Microporous Mesoporous Mater.* 168, 92–101.  
729 <https://doi.org/10.1016/j.micromeso.2012.09.027>

730 van Krevelen, D.W., 1950. Graphical-statistical method for the study of structure and reaction  
731 processes of coal. *Fuel* 29, 269–284.

732 Wang, Q., Li, H., Chen, L., Huang, X., 2001. Monodispersed hard carbon spherules with  
733 uniform nanopores. *Carbon* 39, 2211–2214. [https://doi.org/10.1016/S0008-](https://doi.org/10.1016/S0008-6223(01)00040-9)  
734 [6223\(01\)00040-9](https://doi.org/10.1016/S0008-6223(01)00040-9)

735 Weckhuysen, B.M., Rosynek, M.P., Lunsford, J.H., 1998. Characterization of surface carbon  
736 formed during the conversion of methane to benzene over Mo/H-ZSM-5 catalysts.  
737 *Catal. Lett.* 52, 31–36.

738 Weidenthaler, C., Lu, A.-H., Schmidt, W., Schüth, F., 2006. X-ray photoelectron  
739 spectroscopic studies of PAN-based ordered mesoporous carbons (OMC).  
740 *Microporous Mesoporous Mater.* 88, 238–243.  
741 <https://doi.org/10.1016/j.micromeso.2005.09.015>

742 White, R.J., Antonietti, M., Titirici, M.-M., 2009. Naturally inspired nitrogen doped porous  
743 carbon. *J. Mater. Chem.* 19, 8645. <https://doi.org/10.1039/b911528e>

744 Zhao, L., Baccile, N., Gross, S., Zhang, Y., Wei, W., Sun, Y., Antonietti, M., Titirici, M.-M.,  
745 2010. Sustainable nitrogen-doped carbonaceous materials from biomass derivatives.  
746 *Carbon* 48, 3778–3787. <https://doi.org/10.1016/j.carbon.2010.06.040>

747 Zhao, Y., Li, W., Zhao, X., Wang, D.P., Liu, S.X., 2013. Carbon spheres obtained via citric  
748 acid catalysed hydrothermal carbonisation of cellulose. *Mater. Res. Innov.* 17, 546–  
749 551. <https://doi.org/10.1179/1433075X13Y.0000000108>

750 Zhou, J., Lian, J., Hou, L., Zhang, J., Gou, H., Xia, M., Zhao, Y., Strobel, T.A., Tao, L., Gao,  
751 F., 2015. Ultrahigh volumetric capacitance and cyclic stability of fluorine and nitrogen  
752 co-doped carbon microspheres. *Nat. Comm.*, 6, 8503.  
753 <https://doi.org/10.1038/ncomms9503>

754

755

756 Synthesis and properties of porous carbons based on tannin-sucrose mixtures treated in  
757 hydrothermal conditions  
758 Sanchez-Sanchez et al.

759

760 Captions of the Figures

761 **Fig. 1:** Main flavonoid unit contained in Mimosa tannin extract.

762 **Fig. 2:** Changes of HTC yield of H0S100T180 and H50S50T180 hydrochars obtained at  
763 different pH, and BET areas of the corresponding carbons after subsequent pyrolysis at 900°C  
764 (dashed lines are just guides for the eye).

765 **Fig.3:** Typical SEM images of carbon materials (i.e., pyrolysed at 900°C) based on: tannin  
766 (CH0S100T) and sucrose (CH100S0T) submitted to HTC at 180°C with, a) and b)  
767 unmodified pH and d) and e) pH 2, respectively; based on 50S50T samples submitted to HTC  
768 at 180°C with c) unmodified pH and f) pH 2; and finally based on 50S50T samples submitted  
769 to HTC at pH 2 g) at 160°C and h) 200°C.

770 **Fig. 4:** Total carbon yield and BET area of HTC materials (H50S50T) prepared at different  
771 HTC temperatures (160, 180 and 200°C) at unmodified pH and pH 2, and of pyrolysed  
772 (900°C) CH50S50T carbons.

773 **Fig. 5:** Typical SEM images of carbon materials (i.e., pyrolysed at 900°C) based on sucrose  
774 and tannin mixed in proportions ranging from 25-75 to 100-0 (from left to right) and  
775 submitted to HTC at unmodified pH (a, b, c) and pH 2 (d, e, f).

776 **Fig. 6:** a) HTC yield of materials made at 180°C at different T/S proportions and of  
777 CH50S50T samples prepared at 160 and 200°C; b) Corresponding BET areas  $A_{BET}$  after HTC  
778 and subsequent pyrolysis at 900°C. The dashed lines in a) were calculated (see text), and are  
779 just guides for the eye in b).



780 Fig. 7: BET areas  $A_{BET}$  (open symbols) and product Total carbon yield  $\times A_{BET}$  (full symbols)  
781 as a function of the total carbon yield for materials at different T/S proportions after HTC at  
782 180°C and subsequent pyrolysis at 900°C.

783 Fig. 8: a) Nitrogen adsorption-desorption isotherms (full and open symbols, respectively) at -  
784 196°C for CH50S50T180\_2 and CH50S50T180\_u samples; and b) their pore size  
785 distributions determined by the DFT method (slit-like pore geometry).

786 Fig. 9: a) Van Krevelen diagram for all materials before (100S0T and 0S100T) and after HTC  
787 (H100S0T and H0S100T) at 160, 180 and 200°C, at unmodified pH (HsStT\_u) and at pH 2  
788 (HsStT\_2) and posterior pyrolysis at 900°C (HTC\_900°C); and b) total amounts of CO and  
789 CO<sub>2</sub> gases produced during TPD analysis for materials after HTC at 180°C at different weight  
790 fractions of tannin.

791 Figure 10. Cyclic voltammetry (CV) results obtained in a three-electrode cell in 1 mol L<sup>-1</sup>  
792 H<sub>2</sub>SO<sub>4</sub> electrolyte: (a) CV curves recorded at 0.5 mV s<sup>-1</sup> scan rate; (b) CV curves recorded at  
793 10 mV s<sup>-1</sup> scan rate; (c) Specific capacitance of the samples at scan rates between 0.5 and 100  
794 mV s<sup>-1</sup>; (d) Capacitance retention at scan rates between 0.5 and 100 mV s<sup>-1</sup>.

795 Figure 11. Cyclic voltammetry (CV) results obtained in a three-electrode cell in 1 mol L<sup>-1</sup>  
796 H<sub>2</sub>SO<sub>4</sub> electrolyte: (a, c, e) CV curves recorded at 0.5 mV s<sup>-1</sup> scan rate for the first cycle,  
797 showing the redox peaks on both anodic and cathodic branches; (b, d, f) Evolution of the  
798 potential difference ( $\Delta E$ ) between the maxima of the anodic and cathodic peak 1 as a function  
799 of the cycle number; CV curves were recorded at scan rates between 0.5 and 5 mV s<sup>-1</sup> for  
800 C0S100T, and between 0.5 and 2 mV s<sup>-1</sup> for CH50S50T180\_1 and CH50S50T180\_u.

801 Figure 12. (a, c, e) Dependence of the anodic and cathodic peaks currents,  $I_{p,ox}$  and  $I_{p,red}$ , on  
802 the square root of the scan rate,  $s^{1/2}$ ; (b, d, f) Evolution of the peak potentials,  $E_{p,ox}$  and  $E_{p,red}$ ,  
803 versus the natural logarithm of the scan rate,  $\ln s$ .

804 Synthesis and properties of porous carbons based on tannin-sucrose mixtures treated in  
805 hydrothermal conditions

806 Sanchez-Sanchez et al.

807

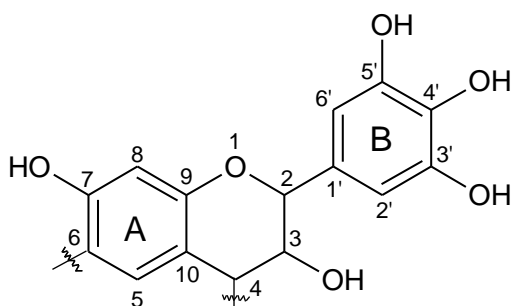
808

809

Figure 1

810

811



812

813

814 Synthesis and properties of porous carbons based on tannin-sucrose mixtures treated in  
815 hydrothermal conditions

816 Sanchez-Sanchez et al.

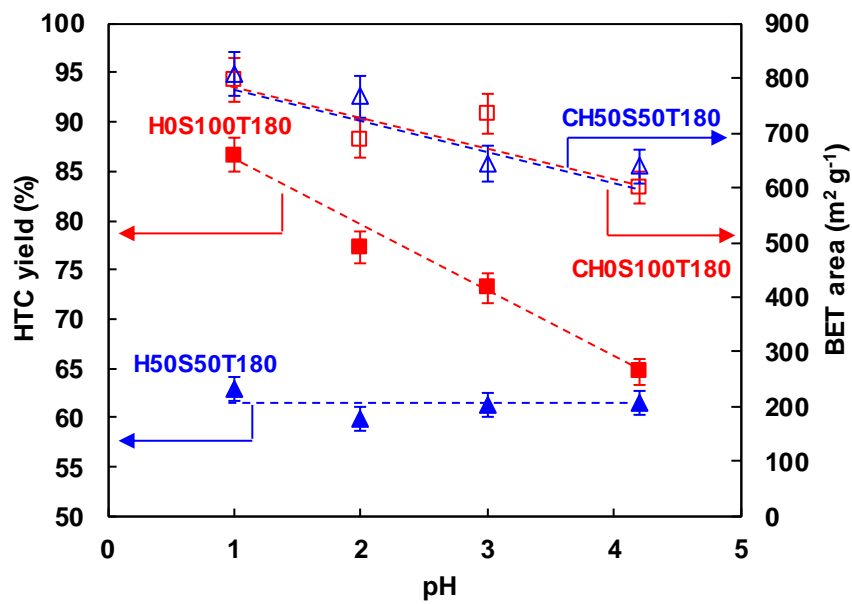
817

818

819

Figure 2

820



821

822

823 Synthesis and properties of porous carbons based on tannin-sucrose mixtures treated in  
824 hydrothermal conditions  
825 Sanchez-Sanchez et al.

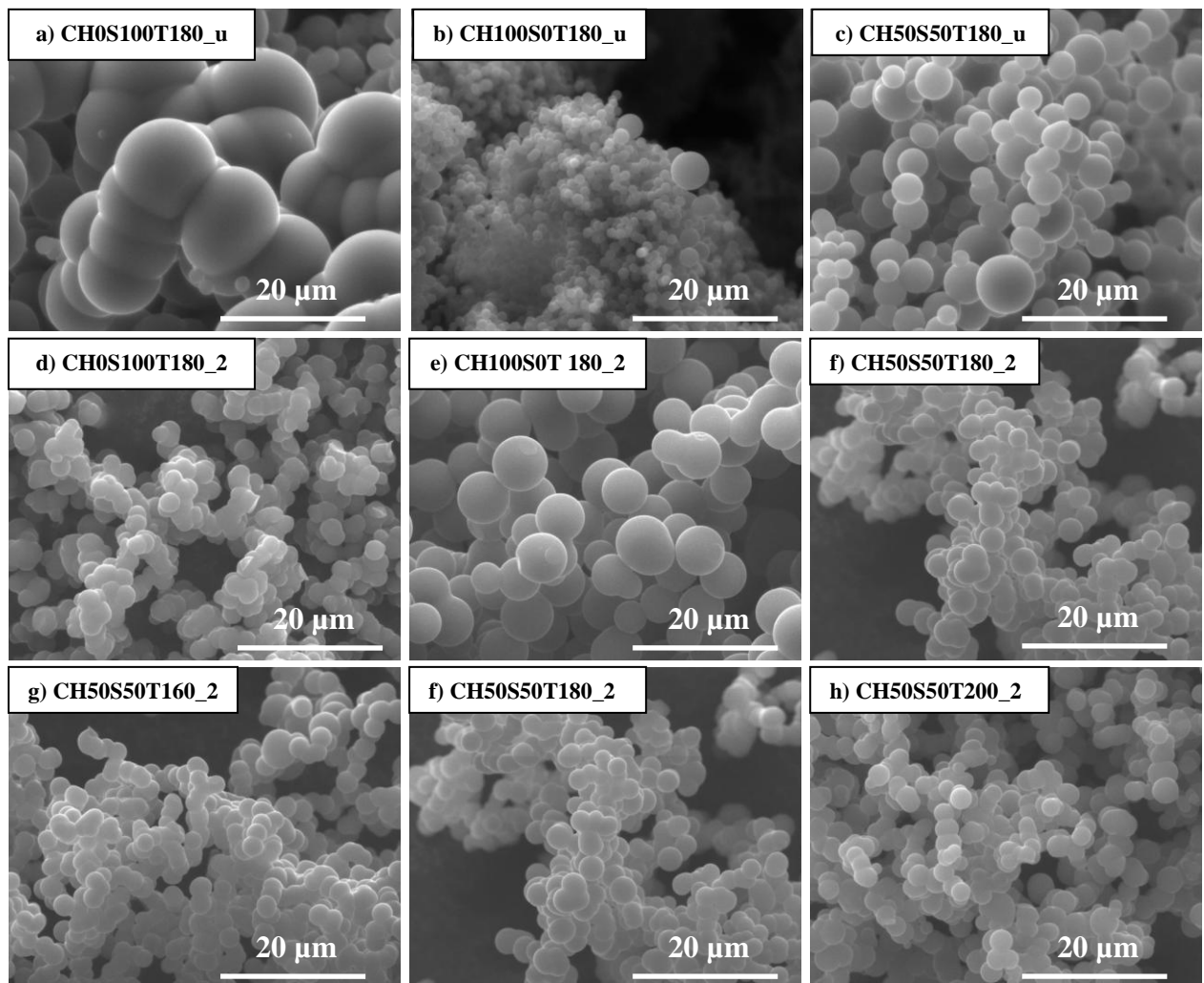
826

827

828

Figure 3

829



830

831

832

833 Synthesis and properties of porous carbons based on tannin-sucrose mixtures treated in  
834 hydrothermal conditions

835 Sanchez-Sanchez et al.

836

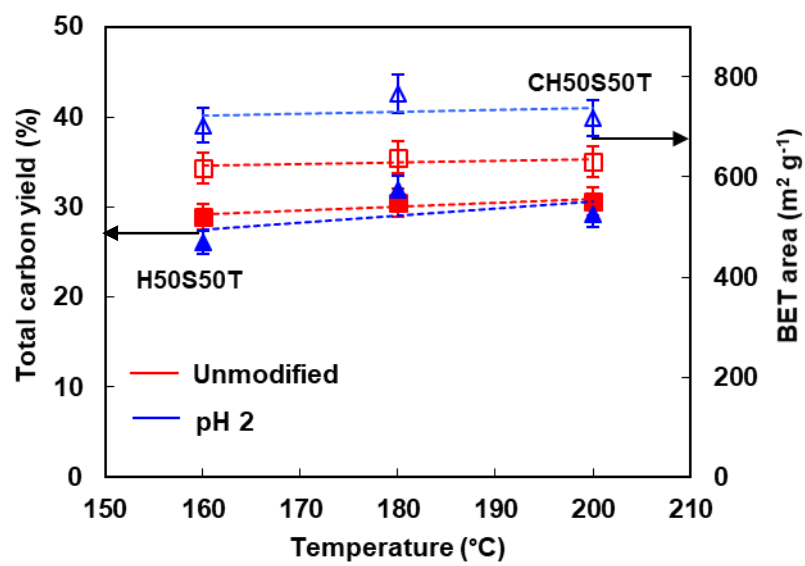
837

838

Figure 4

839

840



846

847

848 Synthesis and properties of porous carbons based on tannin-sucrose mixtures treated in  
849 hydrothermal conditions

850 Sanchez-Sanchez et al.

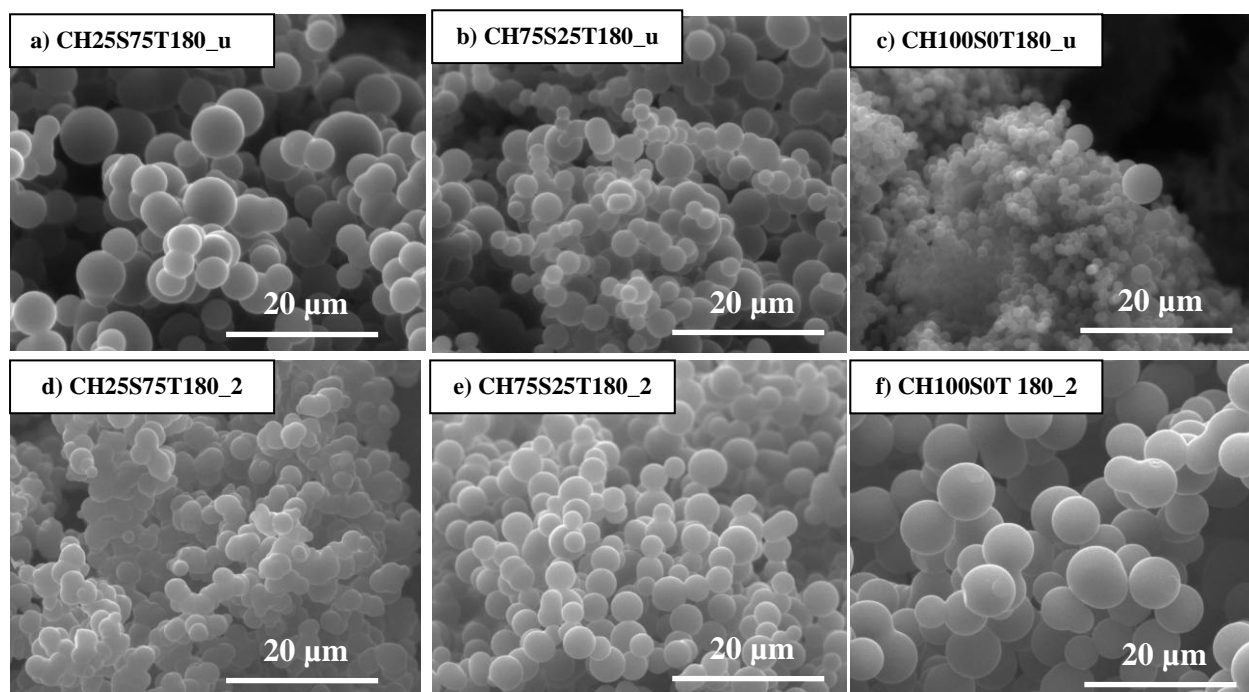
851

852

853

Figure 5

854



855

856

857 Synthesis and properties of porous carbons based on tannin-sucrose mixtures treated in  
858 hydrothermal conditions  
859 Sanchez-Sanchez et al.

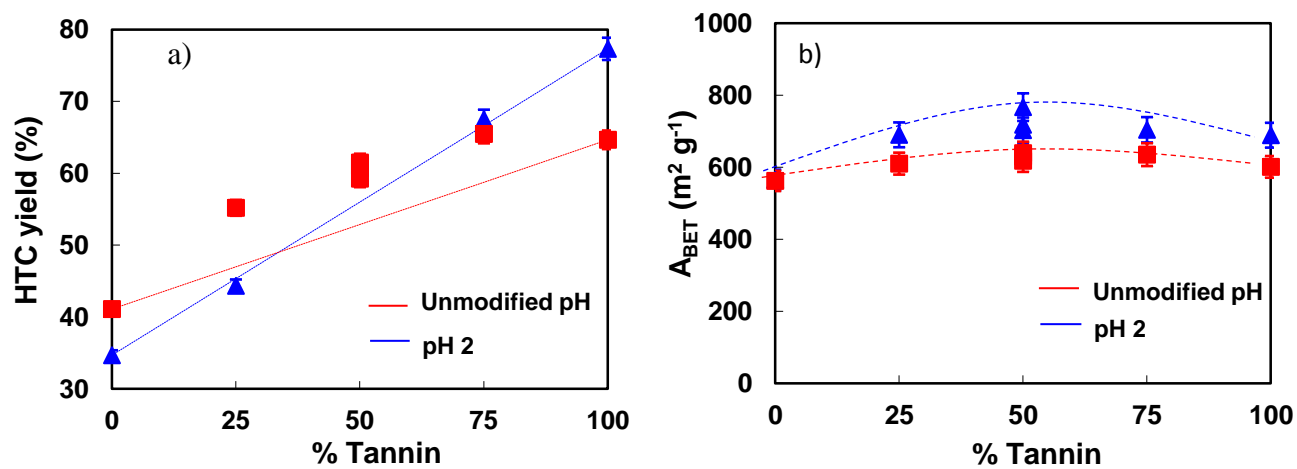
860

861

862

Figure 6

863



864

865

866 Synthesis and properties of porous carbons based on tannin-sucrose mixtures treated in  
867 hydrothermal conditions

868 Sanchez-Sanchez et al.

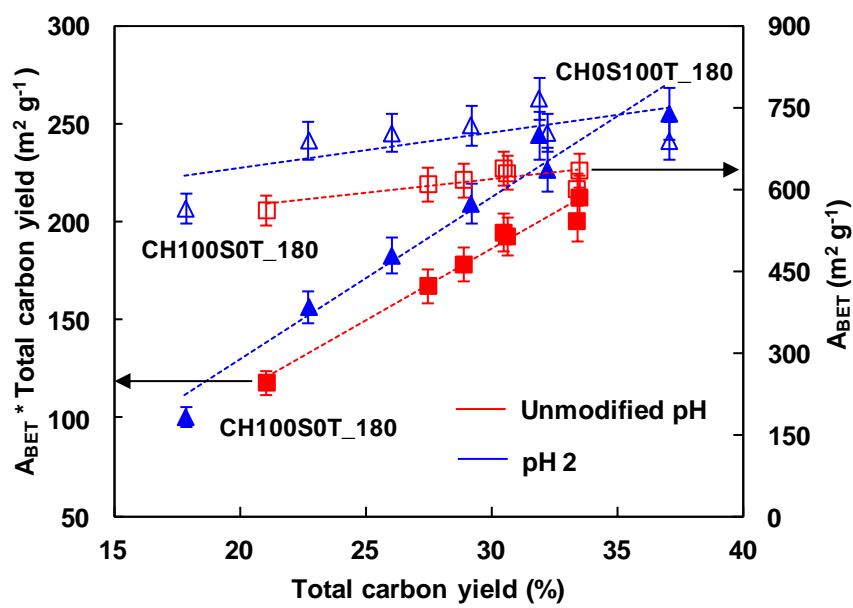
869

870

871

Figure 7

872



873

874



875 Synthesis and properties of porous carbons based on tannin-sucrose mixtures treated in  
876 hydrothermal conditions  
877 Sanchez-Sanchez et al.

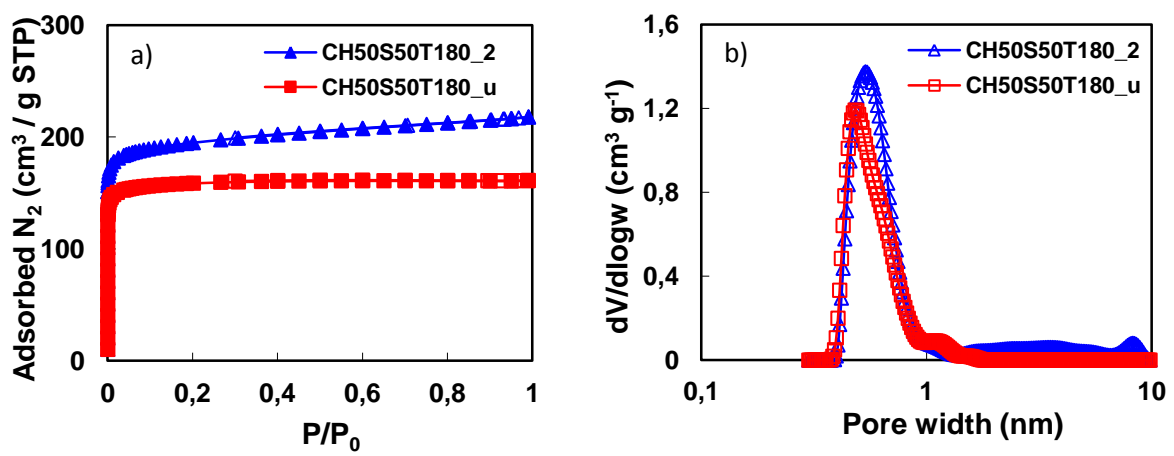
878

879

880

Figure 8

881



882

883

884 Synthesis and properties of porous carbons based on tannin-sucrose mixtures treated in  
885 hydrothermal conditions

886 Sanchez-Sanchez et al.

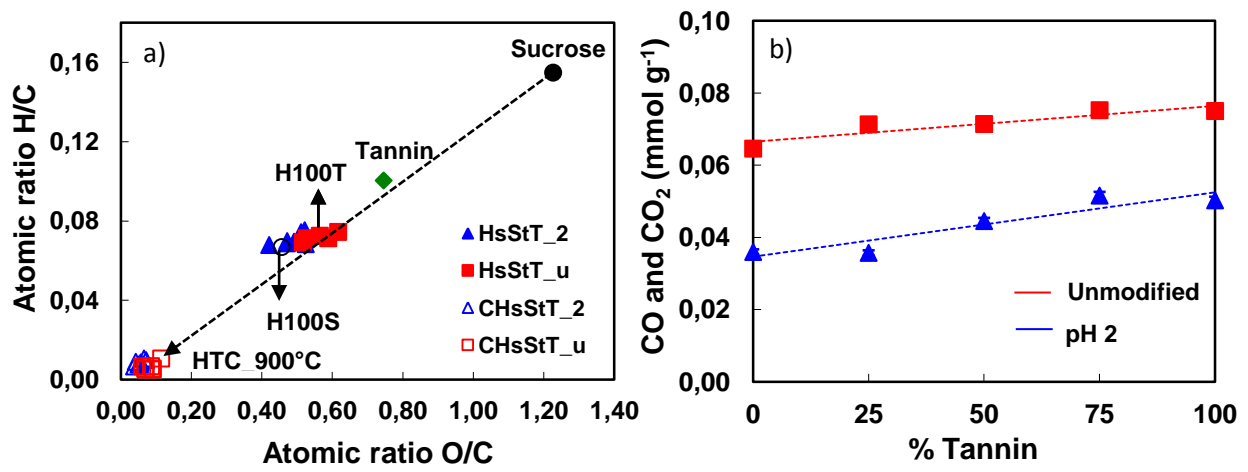
887

888

889

Figure 9

890



891

892

893 Synthesis and properties of porous carbons based on tannin-sucrose mixtures treated in  
894 hydrothermal conditions

895 Sanchez-Sanchez et al.

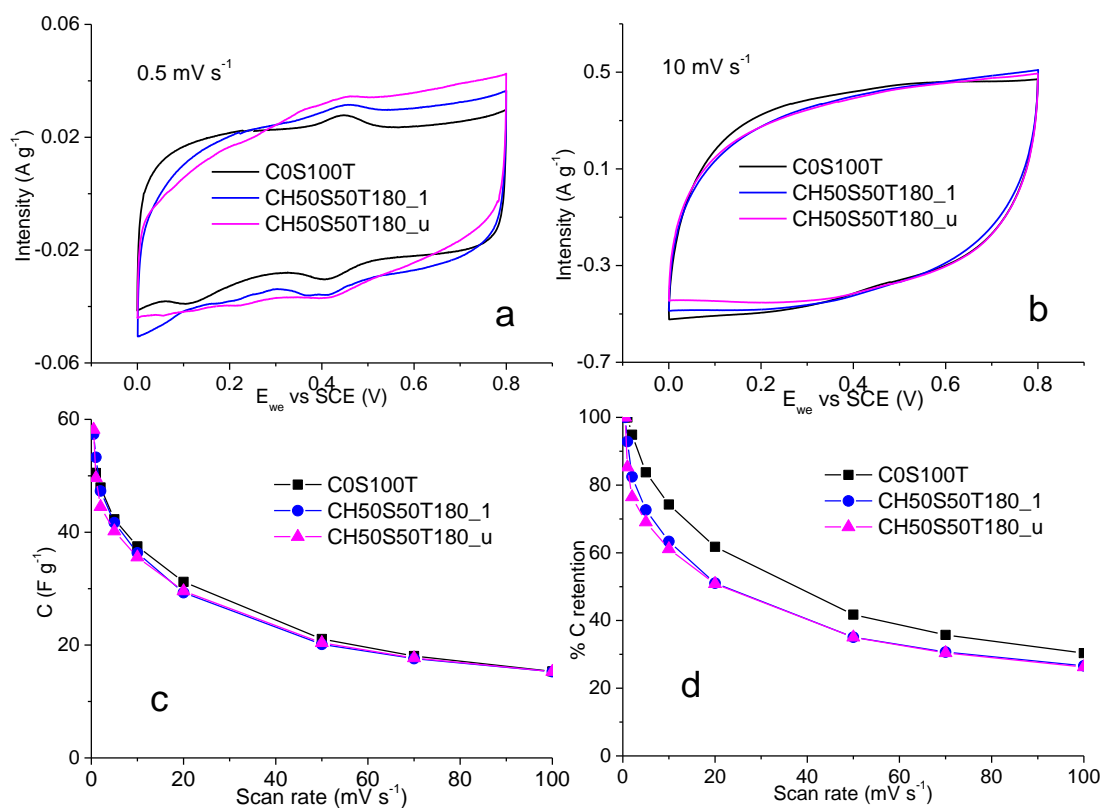
896

897

898

Figure 10

899



900

901

902

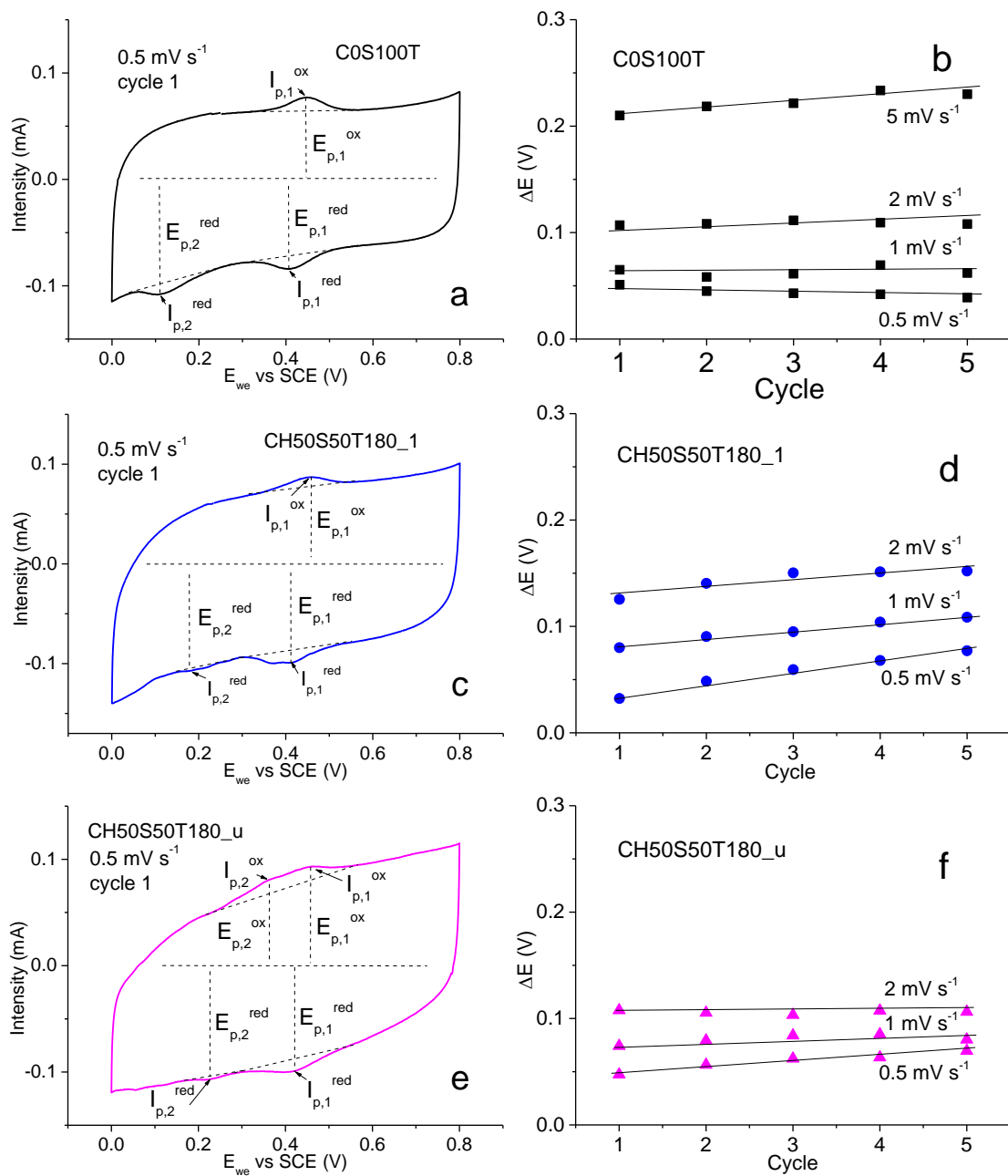
903

907

908

909

Figure 11



910  
911

912 Synthesis and properties of porous carbons based on tannin-sucrose mixtures treated in  
 913 hydrothermal conditions  
 914 Sanchez-Sanchez et al.

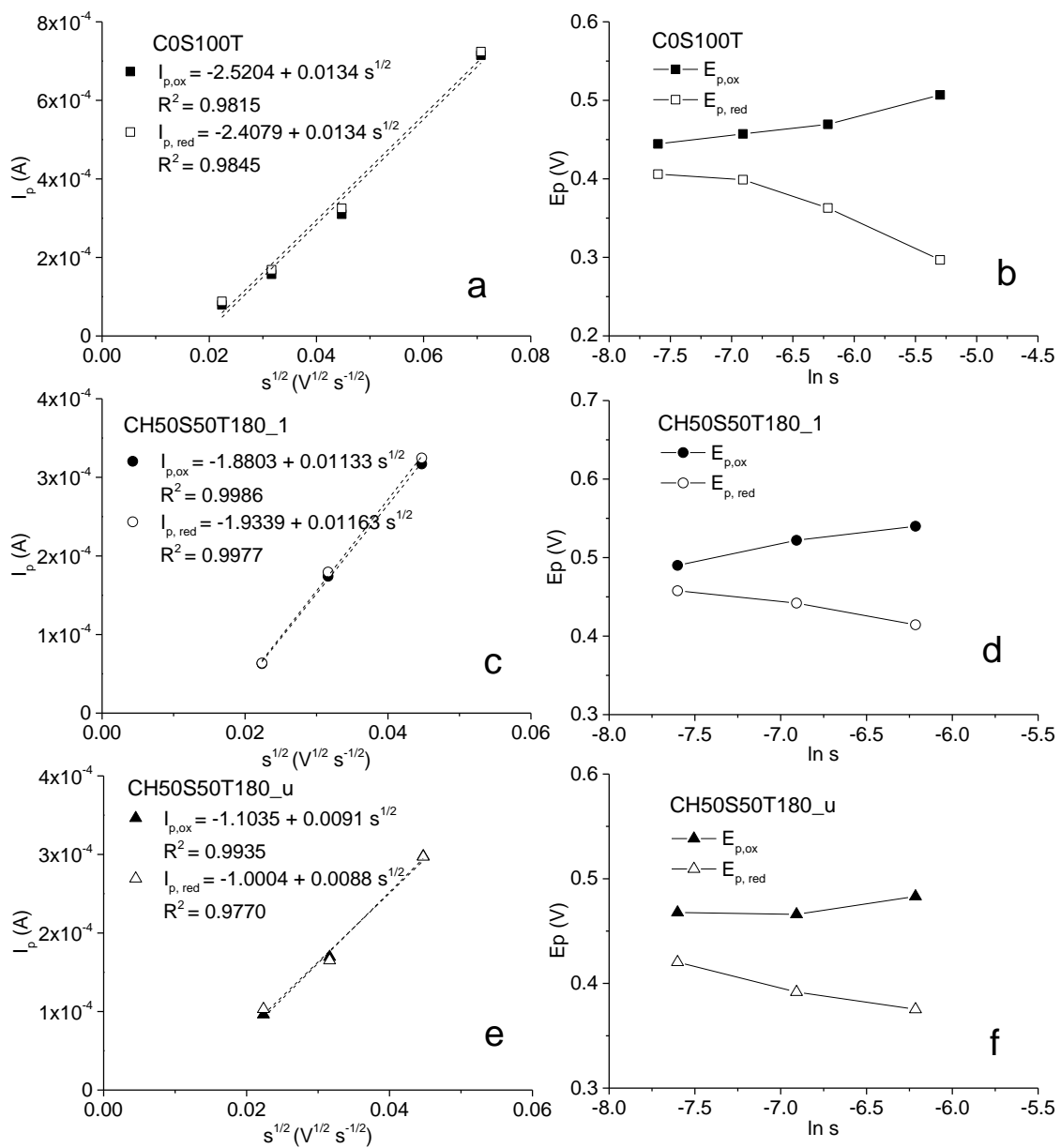
915

916

917

Figure 12

918



919